Constraints on the upper mantle structure beneath the Pacific from 3-D anisotropic waveform modelling

Elodie Kendall[1], Ana M. G. Ferreira[1], Sung-Joon Chang[2], and Daniel B. Peter[3]

[1]University College London
[2]Kangwon National University
[3]King Abdullah University of Science and Technology (KAUST)

November 23, 2022

Abstract

Seismic radial anisotropy is a crucial tool to help constrain flow in the Earth's mantle. However, Earth structure beneath the oceans imaged by current 3-D radially anisotropic mantle models shows large discrepancies. In this study, we provide constraints on the radially anisotropic upper mantle structure beneath the Pacific by waveform modelling. Specifically, we objectively evaluate three 3-D tomography mantle models which exhibit varying distributions of radial anisotropy through comparisons of independent real datasets with synthetic seismograms computed with the spectral-element method. The data require an asymmetry at the East Pacific Rise with stronger positive radial anisotropy ξ=V/V=1.13-1.16 at ˜100km depth to the west of the East Pacific Rise than to the east (ξ=1.09-1.12). This suggests that the anisotropy in this region is due to the lattice preferred orientation of anisotropic mantle minerals produced by shear-driven asthenospheric flow beneath the South Pacific Superswell. Radial anisotropy reduces to ξ=1.09-1.12 beneath the central Pacific and to a minimum of ξ<1.05 in the west, beneath the oldest part of the oceanic lithosphere at ˜100km depth. This reduction in the magnitude of radial anisotropy estimated beneath the west Pacific possibly reflects a deviation from horizontal flow as the mantle is entrained with subducting slabs, a change in temperature or water content that could alter the anisotropic olivine fabric or the shape-preferred orientation of melt. In addition to a lateral age-dependence of anisotropy, our results also suggest that a depth-age trend in radial anisotropy may prevail from the East Pacific Rise to Hawaii (˜90Ma).

Constraints on the upper mantle structure beneath the Pacific from 3-D anisotropic waveform modelling

E. Kendall [1], A.M.G. Ferreira [1,2], S.-J. Chang [3], D. Peter [4]

[1] Department of Earth Sciences, University College London, London, UK 2 CERIS, Instituto Superior Técnico, Universidade de Lisboa, Lisbon, Portugal 3 Division of Geology and Geophysics, Kangwon National University, Chuncheon, South Korea 4 Extreme Computing Research Center, King Abdullah University of Science and Technology (KAUST), Thuwal, Saudi Arabia

Key Points:

- We assess 3-D mantle models of radial anisotropy with full waveform modelling along with independent data
- The data require an asymmetry in radial anisotropy at the East Pacific Rise possibly linked to flow beneath the South Pacific Superswell
- Our new radial anisotropy constraints show a lateral age-dependence, which possibly reflects a change in flow from the horizontal direction

Corresponding author: Elodie Kendall, `elodie.kendall.14@ucl.ac.uk`

Abstract

Seismic radial anisotropy is a crucial tool to help constrain flow in the Earth's mantle. However, Earth structure beneath the oceans imaged by current 3-D radially anisotropic mantle models shows large discrepancies. In this study, we provide constraints on the radially anisotropic upper mantle structure beneath the Pacific by waveform modelling. Specifically, we objectively evaluate three 3-D tomography mantle models which exhibit varying distributions of radial anisotropy through comparisons of independent real datasets with synthetic seismograms computed with the spectral-element method. The data require an asymmetry at the East Pacific Rise with stronger positive radial anisotropy $\xi=\frac{{V_{SH}}^2}{{V_{SV}}^2}$=1.13-1.16 at ∼100 km depth to the west of the East Pacific Rise than to the east (ξ=1.09-1.12). This suggests that the anisotropy in this region is due to the lattice preferred orientation of anisotropic mantle minerals produced by shear-driven asthenospheric flow beneath the South Pacific Superswell. Radial anisotropy reduces to ξ=1.09-1.12 beneath the central Pacific and to a minimum of ξ <1.05 in the west, beneath the oldest part of the oceanic lithosphere at ∼100 km depth. This reduction in the magnitude of radial anisotropy estimated beneath the west Pacific possibly reflects a deviation from horizontal flow as the mantle is entrained with subducting slabs, a change in temperature or water content that could alter the anisotropic olivine fabric or the shape-preferred orientation of melt. In addition to a lateral age-dependence of anisotropy, our results also suggest that a depth-age trend in radial anisotropy may prevail from the East Pacific Rise to Hawaii (∼90 Ma).

Key words: Seismic anisotropy, waveform modelling, mantle flow, Pacific, upper mantle

1 Introduction

Earth's mantle structure has long been investigated through seismic tomography. There is currently large-scale agreement among 3-D isotropic mantle models, at least at shallow depths, such as low seismic wave velocities associated with oceanic ridges and high velocities with cratons (e.g., Chang et al., 2014). Due to the enormous expansion of seismic data sets and advances in computing technology we are also now able to image more complex and realistic properties than isotropy, such as anisotropy and attenuation. In particular, radial anisotropy, the difference between horizontally and vertically polarized shear wave speed ($\xi = \frac{{V_{SH}}^2}{{V_{SV}}^2}$) is a powerful tool to probe the direction of mantle flow. The alignment of mineral grains into a lattice-preferred orientation (LPO) by large-strain deformation such as mantle flow is thought to be the main mechanism behind large scale seismic anisotropy in the upper mantle (e.g., Nicolas and Christensen, 1987; Zhang and Karato, 1995; Karato, 2008). In addition to LPO, another mechanism that can lead to anisotropy is extrinsic anisotropy or shape-preferred orientation (SPO; e.g., Wang et al., 2013) involving the alignment of structural elements, such as, e.g., melt or layers of contrasting elastic properties (e.g. Kendall and Silver, 1996; Faccenda et al., 2019). However, recent 3-D radially anisotropic mantle models built with different data sets, parametrizations and modelling schemes show considerable discrepancies in the geometry and strength of the radial anisotropy (e.g., Chang et al., 2015). A critical example is beneath the oceans, one of the simplest tectonic settings on Earth. Constraints on radial anisotropy in the oceanic upper mantle allow us to explain how deep mantle convection is related to its surface expression. Positive anomalies of radial anisotropy ($V_{SH} > V_{SV}$) currently observed beneath the Pacific oceanic lithosphere are associated to first order with horizontal flow (e.g., Chang et al., 2014). However, the detailed mantle flow patterns in this region are still unknown. For example, some 3-D radially anisotropic mantle models show three distinct linear positive anomalies ($V_{SH} > V_{SV}$) beneath the west coast of South America, the East Pacific Rise and around and to the south of Hawaii (e.g., S362WMANI [Kustowski et al., 2008] and SGLOBE-rani [Chang et al., 2014]; Fig. 1a and b). On the other hand, other models show a smoother region of distributed positive radial anisotropy across the Pacific (e.g., SAVANI [Auer et al., 2014] and SEMUCB-WM1 [French and Romanowicz, 2014]; Fig. 1c and d). This diversity in the strength of radial anisotropy across the Pacific is even more apparent in 1-D profiles through these 3-D radially anisotropic mantle models (Fig. 1e).

Advances in computational power and numerical methods (Olsen et al., 1995; Akcelik et al., 2003; Olsen et al., 2003; Komatitsch and Tromp, 2002) over the last few decades have made large-scale numerical simulations of the seismic wave field in 3-D complex media much more feasible than before. This has opened up the possibility of 3-D full waveform tomography (e.g., Chen et al., 2007a), providing higher resolution constraints on 3-D Earth structure. One of the most widely used and accurate forward modelling approaches, the spectral element method (SEM; Komatitsch and Vilotte, 1998) is being used for such purposes. Fichtner et al. (2009) and Tape et al. (2009) were the first to adopt this approach in regional tomography, in the region of Australasia and Southern California, respectively. In addition, these methods have been applied to image structure in other regions such as the upper mantle beneath the Mid-Atlantic Ridge (Grevemeyer, 2020), beneath East Asia (e.g., Chen et al., 2007b and Chen et al., 2015) and even globally (e.g., French et al., 2013 and Bozdag et al., 2016).

At the global scale, Qin et al. (2008), Qin et al. (2009) and Bozdag and Trampert (2010) used variants of the SEM to test the quality of global tomography models. Qin et al. (2008) and Qin et al. (2009) included 3-D anisotropy in their modelling and used a coupled SEM-normal mode approach (CSEM; Capdeville, 2005) to reduce the computational expense of the calculations. Moreover, Lentas et al. (2013) used the SEM along with global tomography models to test the robustness of earthquake source parameters. At the regional scale, Ni et al. (1999) compared real waveforms with 2D ray-based synthetics to constrain the low-velocity anomaly in the lower mantle beneath Africa. Subsequently, Chu et al. (2012) and Chu et al. (2014) used 3-D SEM modelling to place constraints on the geometry of the Juan de Fuca slab and on the layering of the lithosphere beneath the North America craton, respectively. Furthermore, Thorne et al. (2013) used waveform comparisons to evaluate 1-D and 3-D seismic models of the Pacific lower mantle and Parisi et al. (2018) used SEM modelling to understand the effects of isotropic versus anisotropic lowermost mantle structure on waveforms. However, anisotropic waveform modelling has not been used yet to constrain the anisotropic structure of the oceanic upper mantle.

In this study, we provide constraints on the upper mantle structure of the Pacific by waveform modelling of 3-D anisotropy structure. We use the spectral element method (Komatitsch and Tromp, 2002) to simulate seismic wave propagation for three different 3-D radial anisotropy mantle models that exhibit varying upper mantle distributions of radial anisotropy beneath the Pacific. The synthetic waveforms are compared with independent observed surface waveforms, with the aim of refining the tomographic models. Therefore we pose the questions: How well do current 3-D anisotropic models fit seismic waveform data not used in their construction beneath the Pacific? What adjustments in radial anisotropy are needed for each model to improve the data fit? Is there an age- or depth-dependence to the required radial anisotropy beneath the Pacific?

In the following section we briefly explain the key features and implementation of the Earth models used in this study. The independent data set used and waveform comparison criteria are explained in section 3 and 4, respectively. Our results are outlined and discussed in section 5 and 6, followed by conclusions.

2 Earth models used

As explained in the previous section, some current 3-D tomography models show linear features in radial anisotropy in the Pacific (e.g., S362WMANI and SGLOBE-rani) while others exhibit a smoother, more distributed signature of positive anisotropy. While S36WMANI is already implemented in the SPECFEM3D_GLOBE package (Komatitsch and Tromp, 2002) used in this study and has been extensively tested by the code's developers and users, we add subroutines to the package to implement the mantle structure of SGLOBE-rani. Due to the challenges in matching model parametrization and the spectral element meshing we prefer not to implement models that we did not construct since not knowing the full details of the models' construction, notably how the crust is treated (e.g., Ferreira et al., 2010), may bias their implementation in the SPECFEM3D_GLOBE package. Thus, in order to simulate a smoother anisotropic model we built a new model, SGLOBE-smooth. This model was built using the exact same dataset and modelling scheme as SGLOBE-rani (Chang et al., 2015), but using a regularisation scheme that included both norm damping (as used in the construction of SGLOBE-rani) and horizontal smoothing (i.e., minimising the first derivative of the velocity perturbations). S36WMANI, SGLOBE-rani and SGLOBE-smooth therefore reflect the various possible features of radial anisotropy previously reported in the literature for the region (Fig.1 and Fig. S1 in the supplementary materials). Therefore, we use the following global 3-D mantle models in the seismic waveform simulations: (i) S362WMANI (Kustowski et al., 2008); (ii) SGLOBE-rani (Chang et al., 2015) and (iii) SGLOBE-smooth.

All tomographic mantle models use crustal corrections based on CRUST2.0 (Bassin et al., 2000). Moreover, when building SGLOBE-rani, Chang et al. (2015) also inverted for crustal thickness variations with respect to CRUST2.0 by including short-period group-velocity dispersion measurements from Ritzwoller and Levshin (1998). Therefore, for the SGLOBE-rani and SGLOBE-smooth models we include the crustal thickness variations with respect to CRUST2.0 in the SPECFEM3D_GLO-BE package.

In our waveform modelling we use the same P-wave speed and density models that were employed in the construction of the tomography models used in this study. Hence, S362WMANI is implemented using the following scaling relations for V_P: $\frac{\delta V_{PV}}{V_{PV}} = 0.55\frac{\delta V_{SV}}{V_{SV}}$, $\frac{\delta V_{PH}}{V_{PH}} = 0.55\frac{\delta V_{SH}}{V_{SH}}$ and using the density profile defined by STW105 (Kustowski et al., 2008). On the other hand, SGLOBE-rani and SGLOBE-smooth are implemented using the following scaling relations: $\frac{\delta V_P}{V_P} = 0.5\frac{\delta V_S}{V_S}$ and $\frac{\delta \rho}{\rho} = 0.4\frac{\delta V_S}{V_S}$.

3 Data

We consider 36 earthquakes to study the Pacific that occurred from 2005-2018 recorded at over 1,125 different stations from 92 networks (Table 1). The vast majority of the events (31 out of 36) are chosen after 2009 so that they are independent, i.e., they were not used in the construction of the tomographic models assessed in this study.

Moreover, events are selected with Mw>5 to ensure a good signal to noise ratio but below Mw 7 to prevent substantial finite-source effects. Shallow earthquakes with a hypocentral depth <50 km are chosen to reduce the excitation of surface wave overtones. For each event, we download 90 minute-long three-component broadband waveforms from IRIS (`https://www.iris.edu/hq/`) recorded within an epicentral distance of 10-120° to avoid near-source effects, caustics and multiple orbit overlapping phases.

We deconvolve the instrument's response, rotate the horizontal components into radial and transverse components, resample the data to 1 s, remove the median and trend and apply a Butterworth-bandpass filter of order 4 with the dominant wave periods of T$\sim$40, 60 and 100 s (corner frequencies: 0.021-0.031 Hz, 0.014-0.021 Hz and 0.013-0.008 Hz, respectively) to isolate Rayleigh and Love waves with these dominant periods. The surface wave sensitivity kernels (supplementary materials, Fig. S2) show that fundamental mode Rayleigh waves with dominant wave periods of 40, 60 and 100 s have peak sensitivity to radially anisotropic mantle structure at depths around 40-100, 60-120 and 80-200 km, respectively (supplementary materials, Fig. S2a). On the other hand, fundamental mode Love waves have broader and shallower sensitivity in the mantle than Rayleigh waves, such that when filtered with dominant wave periods of 40, 60 and 100 s, Love waves have good sensitivity to around 30-70, 40-110 and 50-150 km depths, respectively (supplementary materials, Fig. S2b).

4 Waveform comparisons and model adjustments

We use the SPECFEM3D_GLOBE package (Komatitsch and Tromp, 2002) to simulate the global seismic wavefield for the various tomographic models discussed above. We use 256 spectral elements along each side of a chunk in the cubed sphere of the mesh such that synthetic seismograms are accurate down to T$\sim$17 s. A point source model is used with source parameters from the GCMT catalogue (`https://www.globalcmt.org/CMTsearch.html`).

We process the data and corresponding synthetic seismograms in exactly the same way (see previous section). We then isolate the fundamental mode surface waves by windowing the waveforms around the maximum amplitude of the data (with a width of 2.5 times the dominant wave period to encapsulate the phase and avoid the interference of surface wave overtones). We then calculate phase misfits, $\Delta\phi$ for both Rayleigh and Love waves and for each dominant wave period by cross-correlation between the real and synthetic waveforms whereby positive/negative phase misfits correspond to the synthetic waveforms being faster/slower than the observed waveforms. In addition, amplitude misfits are calculated using the following equation,

$$\Delta \mathrm{A} = \ln \sqrt{\frac{\sum_i {A^i_{\mathbf{real}}}^2}{\sum_i {A^i_{\mathbf{synthetic}}}^2}}, \tag{1}$$

which shows the logarithmic ratio between the summed real, $\mathrm{A}_{\mathrm{real}}$ and synthetic, $\mathrm{A}_{\mathrm{synthetic}}$ amplitudes for each data window.

In order to exclude obvious outliers from the analysis, waveforms are accepted if the cross-correlation value between the data and synthetics exceeds 0.7, the absolute phase misfit is smaller than 40 s and if the amplitude misfit is between -3 and 3. This leads to a total of 2,307 waveform comparisons. The corresponding source-receiver distributions and great-circle paths are shown in Fig. 2.

After quantifying the misfits between the data and synthetics, we estimate the first-order adjustments in radial anisotropy in the 3-D models that are required to improve the data fit for each path. Most of the current whole-mantle models (e.g., Ritsema et al., 2011; Auer et al., 2014; Moulik and Ekström, 2014; Chang et al., 2015) use the so-called great-circle approximation (GCA), an infinite frequency ray theory approach that only takes first-order path effects into account (Woodhouse and Dziewonski, 1984) to calculate body-wave traveltimes and surface wave phases. Low computational costs associated with this method along with the use of massive datasets may partly compensate the theory's limitations. Moreover, Parisi and Ferreira (2016) reported that the GCA accurately predicts surface wave phase for T∼45-150 s for current global tomography models. According to the GCA, the phase misfit between real and theoretical seismograms for a fundamental mode Rayleigh or Love wave for a given path can be written as:

$$\begin{aligned}\Delta\phi(\omega) &= \int \left(\frac{1}{C_{\mathrm{real}}(\omega)} - \frac{1}{C_{\mathrm{synthetic}}(\omega)}\right)\mathrm{dl} \\ &= \left(\frac{1}{C_{\overline{\mathrm{real}}}(\omega)} - \frac{1}{C_{\overline{\mathrm{synthetic}}}(\omega)}\right) \times \Delta\end{aligned} \tag{2}$$

where the integral is computed along the source-receiver great-circle path, l, Δ is the source-receiver epicentral distance and $\mathrm{C}_{\overline{\mathrm{real}}}(\omega)$ and $\mathrm{C}_{\overline{\mathrm{synthetic}}}(\omega)$ are the average along-path phase velocities of the real and synthetic waveforms, respectively, which depend on the angular frequency, ω. $\mathrm{C}_{\overline{\mathrm{synthetic}}}(\omega)$ can be computed using a normal mode formalism (Gilbert, 1971). We compute normal mode eigenfrequency catalogues with the mineos package `https://geodynamics.org/cig/software/mineos/` for the 1-D source-receiver average structure calculated from the 3-D Earth model considered. Hence, using $C_{\overline{\mathrm{synthetic}}}(\omega)$, the measured phase misfit $\Delta\phi(\omega)$ and the epicentral distance Δ, the real average phase velocity of each fundamental mode surface wave can then be estimated as,

$$C_{\overline{\mathrm{real}}}(\omega) = \frac{1}{\frac{\Delta\phi(\omega)}{\Delta} + \frac{1}{C_{\overline{\mathrm{synthetic}}}(\omega)}}. \tag{3}$$

Once $C_{\overline{\mathrm{real}}}(\omega)$ is computed with Eq. 3, we can then systematically vary $\mathrm{V_{SH}}$ and $\mathrm{V_{SV}}$ and compute the theoretical phase velocities of Rayleigh and Love waves until a good agreement with the actual real phase velocity $C_{\overline{\mathrm{real}}}(\omega)$ is achieved. For Love waves with a dominant wave period of T∼40 s, 60 s and 100 s we uniformly modify the corresponding $\mathrm{V_{SH}}$ profiles in the average model every 10 km between 30-70, 40-110, 50-150 km depth, respectively. For Rayleigh waves, we uniformly modify the corresponding $\mathrm{V_{SV}}$ profiles in the average model every 10 km between 40-100, 60-120 and 80-200 km depth, respectively. By uniformly changing the shear velocity structure in these depth ranges we obtain a first order estimate of the adjustments in radial anisotropy needed. Previous studies have shown that fundamental mode Rayleigh and Love waves are primarily sensitive to V_{SV} and V_{SH}, respectively, and that it is appropriate to constrain V_{SV} and V_{SH} separately when using fundamental mode data (e.g., Ekström and Dziewoński, 1998; Visser et al., 2008), which justifies our approach.

5 Results

5.1 Illustrative waveform examples

Figure 3 shows an illustrative example of surface waveforms for a path from south Kermadec to north America. For this specific path, positive Rayleigh wave phase misfits of more than 5 s (Fig. 3 Z comp., T$\sim$60 s) indicate that all 3-D global anisotropic models lead to faster Rayleigh waves than the data and that adjustments in radial anisotropy are required to improve the data fit. Moreover, negative Love wave phase misfits around 10 s (Fig. 3 T comp., T$\sim$60 s) show that S362WMANI leads to slower Love waves than the data for this path.

5.2 Surface wave phase misfits

Fig. 4 shows the distributions of phase misfits for all the paths shown in Fig. 2 for each of the 3-D global anisotropic models used in this study. As seen in the illustrative example above, as period increases the phase misfit distributions get narrower and with lower medians, with the lowest misfits occurring for T$\sim$100 s waves, which have maximum sensitivity around $\sim$150 km depth (Fig. 4, bottom). On the other hand, the largest misfits occur for T$\sim$40 s, which have greater sensitivity to shallower depths and to the crust (Fig. 4, top). SGLOBE-smooth leads to the poorest Love wave phase misfits, whereby synthetic Love waves are on average 3-4 s faster than the data (Fig. 4; T comp., T$\sim$40 s, 60 s; red). On the other hand, S362WMANI (Fig. 4; T comp., T$\sim$40 s, blue) and SGLOBE-rani (Fig. 4; T comp., T$\sim$40 s, green) lead to Love waves that fit the data well, with a median phase misfit of <2.5 s. Regarding Rayleigh waves, S362WMANI fits the data slightly better than SGLOBE-rani and SGLOBE-smooth, with the two latter models showing median misfits of $\sim$3.5-4 s for T$\sim$40 s and T$\sim$60 s, respectively (Fig. 4; Z comp).

Fig. 5 shows the geographical distribution of the phase misfits obtained for Love (middle row) and Rayleigh (bottom row) waves at T$\sim$60 s, which are mostly sensitive to $\sim$100 km. S362WMANI fits Love wave data well within 10 s except for paths from Tonga-Kermadec to North America. When considering the model SGLOBE-rani, which shows stronger, positive radially anisotropic anomalies along and around this path than S362WMANI, synthetic

Love waves fit the data within 10 s (Fig. 5b, middle). Finally, the model with strong and smooth radial anisotropy beneath most of the Pacific (SGLOBE-smooth) leads to synthetic Love waveforms that are often faster than the data by 10 s near the East Pacific Rise (EPR), South America and for paths between Tonga-Kermadec and North America (Fig. 5c, middle). In terms of Rayleigh waves, S362WMANI fits the data well within 10 s except for synthetic Rayleigh waves more than 10 s faster than the data to the west of the EPR (Fig. 5a, bottom). A similar pattern of phase misfits can be found for SGLOBE-rani and SGLOBE-smooth, which also lead to synthetic Rayleigh waves more than 10 s faster than the data for paths from Tonga-Kermadec to North America (Fig. 5b-c bottom).

Note that similar trends can be seen in the Rayleigh and Love phase misfits at T$\sim$40 s, which have main sensitivity around $\sim$60 km depth (supplementary materials, Fig. S3). As the wave period increases to T$\sim$100 s (with main sensitivity around $\sim$150 km depth), the phase misfits become very low in the whole region (Fig. S4 in the supplementary information). This is again likely due to the less heterogeneous media being sampled.

5.3 Adjustments in upper mantle radial anisotropy

Using the procedure described in section 4 and the phase misfits presented above (Fig. 5), we estimate the real phase velocity of the surface waves (Fig. 6 and supplementary materials, Fig. S5 and Fig. S6; first and fourth row for Love and Rayleigh waves, respectively). We systematically vary $\mathrm{V_{SH}}$ and $\mathrm{V_{SV}}$ until the adjusted synthetic Love and Rayleigh wave phase velocities are consistent with the real phase velocities, leading to differences mostly smaller than 0.1% (Fig. 6 and supplementary materials, Fig. S5 and Fig. S6; second and fifth row for Love and Rayleigh wave phase velocities, respectively). Using the best-fitting $\mathrm{V_{SH}}$ and $\mathrm{V_{SV}}$ profiles, the adjustments in radial anisotropy required by the data with respect to the original anisotropy in the various models considered are then computed (Fig. 7).

Fundamental mode Love waves are mostly sensitive to V_{SH} and therefore synthetic Love waves slower than the data would indicate that the radial anisotropy in the model considered ($\xi = \mathrm{V_{SH}}^2/\mathrm{V_{SV}}^2$) is too low. In agreement with the slow Love wave synthetics of S362WMANI along paths from Tonga-Kermadec to North America shown e.g. in Fig. 5, we find that the data require an increase in anisotropy of $\sim$3-5% in this region (Fig. 7a middle row). Fundamental mode Rayleigh waves are mostly sensitive to V_{SV} and therefore synthetic Rayleigh waves faster than the data would indicate that the radial anisotropy is too low in the model considered. Therefore, the fast Rayleigh wave synthetics of S362WMANI west of the EPR shown e.g. in Fig. 5 mean that the data require an increase in anisotropy of $\sim$4-6% in this region.

The fast Rayleigh wave synthetics of SGLOBE-rani in paths west of the EPR and between Tonga-Kermadec and North America (e.g., Fig. 5) suggest that the data require an increase in anisotropy of ∼4-6% and 1-3% in these regions, respectively (Fig. 7b middle). Likewise, the fast Rayleigh wave synthetics of SGLOBE-smooth west of the EPR and between Tonga-Kermadec and North America (Fig. 5) imply that the data require an increase in anisotropy of ∼2-3% and 0-1% in these regions, respectively (Fig. 7c middle). The data also suggest that radial anisotropy in SGLOBE-smooth is too high and that a reduction of ∼2-4% is required in the south Pacific. A similar pattern but larger anisotropic perturbations are found in the analysis at T∼40 s (Fig. S7). At longer periods, such as T∼100 s, as expected, the data require smaller adjustments in radial anisotropy (Fig. S8).

To summarise our findings, the bottom row in Fig. 7 shows the distribution of absolute average along-path radial anisotropy for each model after the adjustments in radial anisotropy required by the data have been made. We find good agreement among these adjusted anisotropic models, which show that the data require ξ to be 1.09-1.12 ($d\xi/\xi$=3-6% with respect to PREM) beneath the west coast of South America, 1.13-1.16 ($d\xi/\xi$=6-9% with respect to PREM) west of the EPR and 1.09-1.12 beneath the central-Pacific. Radial anisotropy then reduces further to ξ =1.05-1.1 ($d\xi/\xi$=0-4% with respect to PREM) in the northwestern Pacific and to a minimum of ξ <1.05 in the west Pacific at ∼100 km depth.

In addition to verifying agreement between the real and synthetic phase velocities (third and sixth rows in Fig. 6) we also cross-check our technique of estimating the adjustments in the models needed by checking that the corresponding Voigt averages (${V_{\mathrm{Voigt}}}^2 = \frac{2{V_{SV}}^2+{V_{SH}}^2}{3}$) have not been drastically perturbed (supplementary materials, Figs. S9, S10 and S11).

6 Discussion

Rather than building a new anisotropic model, we used independent waveform modelling to analyse the robustness of radially anisotropic features in existing tomography models in the upper mantle beneath the Pacific. We presented comparisons of surface waves in real independent waveforms with highly accurate synthetics computed for 3-D radially anisotropic mantle models. Furthermore, we presented average, along-path estimates of the adjustments required in the radial anisotropy models in an attempt to better constrain upper mantle anisotropy structure, which is key for more accurate interpretations in terms of mantle flow.

Our analysis showed that surface wave phase misfits are in the range of about ±15 s for T∼60 s waves (Fig. 4 and 5), which require adjustments of up to 6% in the radial anisotropy of the 3-D mantle models considered (Fig. 7 middle). In particular, the region close to the

EPR requires the largest adjustments of up to ∼6% in radial anisotropy across the three anisotropic models (Fig. 7 middle). This correlates well with synthetic resolution tests by Chang et al. (2015) (Fig. 16 in their study) which show a slightly poorer recovery of the amplitude of anisotropic anomalies in the young, eastern Pacific compared with the rest of the Pacific. Therefore the underestimated radially anisotropic anomalies near the EPR are likely the result of poor data coverage. To improve the retrieval of radially anisotropic anomalies in the Pacific, particularly west of the EPR and beneath the central Pacific, it is essential to incorporate data from ocean bottom seismometers (OBSs) such as the Pacific Array (Kawakatsu, 2016) into future data sets.

In this study we found that the data require strong, positive ($V_{SH} > V_{SV}$) lateral variations in radial anisotropy up to ξ ∼1.6 at ∼100 km depth (Fig. 7 bottom). These findings confirm previous reports since the 1980's of faster SH anomalies in the upper few hundred kilometres beneath the Pacific (e.g., Cara and Lévêque, 1988; Nishimura and Forsyth, 1989; Montagner and Tanimoto, 1991; Ekström and Dziewoński, 1998; Gung et al., 2003; Nettles and Dziewoński, 2008; Burgos et al., 2014; Beghein et al., 2014; Isse et al., 2019).

The data require strong ξ of 1.09-1.12 at ∼100 km depth beneath the west coast of South America. The Andean margin can be subdivided into five main tectonic segments, comprising regions with normal subduction and flat subduction. Azimuthal anisotropy in this region has been detected and widely studied for decades (e.g., Eakin and Long, 2013; Eakin et al., 2014; Eakin et al., 2015). For example, local S-wave splitting observations suggest that the mantle above the Peruvian flat slab is anisotropic, with modest average delay times of 0.28 s that are consistent with 4% anisotropy in a 40 km thick mantle layer (Eakin et al., 2014). The majority of fast directions align trench-parallel, as often found in the forearc of subduction zones (Eakin et al., 2014). This corresponds well with the strong, positive radial anisotropy (ξ =1.09-1.12) required in this study and could be linked with horizontal flow in the sub-slab mantle. Moreover, a recent surface wave tomography study incorporating a vast amount of OBS data with a focus beneath the Pacific Ocean by Isse et al. (2019) also images strong, positive radial anisotropy with ξ =1.09-1.12 at ∼75-100 km depth beneath the west coast of South America.

The data indicate that stripes in radial anisotropy between the west coast of South America, the EPR and around and south of Hawaii are hard to distinguish. Despite this, a region with ξ =1.13-1.16 west of the EPR is required by the data. A positive radially anisotropic anomaly near the EPR is consistent with the study of Gu et al. (2005) and Nettles and Dziewoński (2008) in which an anomaly of $d\xi/\xi$ ∼6% at ∼100 km is reported. Moreover, the surface wave tomography study by Isse et al. (2019) which incorporated OBS data also images positive radial anisotropy with ξ >1 at ∼75-100 km depth west of the

EPR. The EPR is the fastest spreading ridge in the world and strongly deforming horizontal mantle flow can lead to the lattice-preferred orientation (LPO) of anisotropic minerals and therefore strong, positive radial anisotropy. The radial anisotropy could also be attributed to the shape-preferred orientation (SPO) e.g. from partial melting (e.g., Tan and Helmberger, 2007, Schmerr, 2012 and Isse et al., 2019). The presence of melt beneath the ridge axis, particularly to the west, is also supported by Baba et al. (2006).

Despite the Pacific and Nazca plate sharing a boundary in the EPR, several studies have found pronounced asymmetry. For example, the Pacific (west) side is characterized by a higher abundance of seamounts (with a source propagating eastwards at $\sim$20 cm/yr; Ballmer et al., 2013), lower S-wave velocities (e.g., Forsyth et al., 1998; Toomey et al., 1998; Dunn and Forsyth, 2003), greater shear-wave splitting (e.g., Wolfe and Solomon, 1998), a higher electrical conductivity (e.g., Evans et al., 1999) and slower subsidence (e.g., Cochran, 1986; Morgan and Smith, 1992; Morgan et al., 1995) than the Nazca (east) side. The required radial anisotropy in the Pacific, as calculated in this study, also shows an asymmetry at the EPR. These results suggest a stronger lattice-preferred orientation (LPO) of anisotropic mantle minerals (e.g., olivine, enstatite) west of the EPR than to the east. This stronger LPO suggests that mantle flow beneath the EPR is not the symmetric corner flow usually assumed in mid-ocean ridge models (e.g., Morgan, 1987). Instead, the stronger LPO could be due to pressure-driven eastern asthenospheric flow from the South Pacific Superswell. This interpretation of the asymmetry across the south East Pacific Rise (e.g., The MELT Seismic Team, 1998) being the result of vigorous, shear-driven eastward asthenospheric flow opposing plate motion is in line with previous studies (e.g., Conder et al., 2002; Toomey et al., 2002; Weeraratne et al., 2007; Ballmer et al., 2013; Lin et al., 2016). Furthermore, this hypothesis has been supported and explained geophysically and geochemically by some numerical models (e.g., Ballmer et al., 2010; Harmon et al., 2011; Ballmer et al., 2013).

Radial anisotropy then reduces with lithospheric age from a strong anomaly of ξ =1.13-1.16 close to the ridge to ξ=1.09-1.12 beneath the central Pacific, which is consistent with Ekström and Dziewoński (1998), Nettles and Dziewoński (2008) and the surface wave tomography study incorporating OBS data by Isse et al. (2019). The paths from Tonga-Kermadec to North America tend to be long, so strictly the path-averaged anomalies could be due to structure other than Hawaii. However, if the $V_{SH} > V_{SV}$ anisotropy along those paths is due to mechanisms occurring beneath Hawaii, one may interpret the radial anisotropy to be caused by LPO due to a plume-lithosphere interaction (e.g., Auer et al., 2015), a change in olivine fabric as the plume dehydrates (e.g., Karato, 2008) and partially melts or due to SPO from partial melt (e.g., Schmerr, 2012, Rychert et al., 2013 and Isse et al., 2019) .

Radial anisotropy then reduces further to ξ =1.05-1.1 at $\sim$100 km depth in the northwestern Pacific, in agreement with Isse et al. (2019), which may reflect the lower levels of deformation beneath the old oceanic lithosphere. In the west, radial anisotropy reduces to ξ <1.05 at $\sim$100 km depth. This lower magnitude of radial anisotropy (a reduction in $V_{SH} > V_{SV}$) could indicate a deviation from horizontal to vertical flow as flow is entrained with subducting slabs, a change in temperature or water content that could alter the anisotropic olivine fabric (Karato, 2008) or SPO from melt.

The strongest positive radial anisotropy at $\sim$100 km in the Pacific lies just west of the EPR (Fig. 7). At a larger depth of 150 km, the 3-D anisotropic models used in this study show strongest positive radial anisotropic anomalies in the central Pacific, beneath older oceanic lithosphere (Fig. S4 top). Fig S4 and S8 show that at larger depths, e.g., at $\sim$150 km depth, synthetic surface waves fit the data well (e.g., S362WMANI and SGLOBE-rani lead to Love and Rayleigh waves that fit the data within 1 s on average) and require small adjustments in perturbations of radial anisotropy (median and standard deviation for each model is 0$\pm$1%). Therefore, although the results are first order path average estimates, the data suggest a depth-age trend in radial anisotropy from the EPR to Hawaii ($\sim$90 Ma) may exist, in agreement with the surface wave tomography study of Isse et al. (2019). This is also consistent with the findings of Beghein et al. (2019), which reported that large uncertainties may be responsible for the apparent lack of depth-age in current global radial anisotropy models.

It is important to note that in order to calculate adjustments in perturbations in radial anisotropy we used 1-D average Earth models across each path and we computed the theoretical phase velocity assuming a spherically symmetric non-rotating Earth. Therefore while e.g. Parisi and Ferreira (2016) showed that this approach is valid for current tomography models and this leads to useful first order estimates of radial anisotropy, it is difficult to assign the patterns recovered to precise regions. Moreover, due to the lack of seismic stations in the Pacific, this dataset comprises relatively long paths and future datasets should include shorter paths to examine smaller regions in the Pacific. Ongoing and future seismic deployments in the region should enable further refined analyses in the future.

7 Conclusions

In this study we constrained the radially anisotropic structure in the Pacific upper mantle by using waveform modelling to assess the robustness of anisotropic features beneath the Pacific in 3-D tomographic mantle models exhibiting varying distributions of radial anisotropy. We compared synthetic SEM seismograms with independent surface waveforms recorded in and around the Pacific. Using the phase misfits for Love and Rayleigh waves, we systematically varied the wave speed of horizontally and vertically polarised shear waves (V_{SH} and V_{SV}), respectively, until a good agreement was found between the theoretical and synthetic phase velocities. The best-fitting V_{SH} and V_{SV} profiles identified allowed a quantification of the adjustments in radial anisotropy required for the 3-D anisotropy models considered. We found that the data require an asymmetry at the East Pacific Rise with stronger positive radial anisotropy ξ=1.13-1.16 at about 100 km depth to the west of the East Pacific Rise than to the east (ξ=1.09-1.12). This asymmetry in radial anisotropy is possibly due to the lattice preferred orientation of intrinsically anisotropic mantle minerals produced by shear-driven asthenospheric flow beneath the South Pacific Superswell. Radial anisotropy reduces to ξ=1.09-1.12 beneath the central Pacific and reduces further to ξ <1.05 beneath the oldest seafloor at ~100 km depth. Lower radial anisotropy could indicate a deviation of the flow direction from horizontal as flow is entrained with subducting slabs, a change in temperature or water content that could alter the olivine fabric or the shape-preferred orientation of melt. In addition to a lateral age-dependence of anisotropy, our results also suggest that a depth-age trend in radial anisotropy may prevail from the East Pacific Rise to Hawaii (~90 Ma).

Acknowledgments

The data for this research is available through the IRIS Data Management Center: `https://www.iris.edu/hq/`. Specifically, we gratefully acknowledge the availability of broadband seismograms including from the IRIS/USGS (IU), the IRIS/IDA Network (II); the GEOSCOPE Network (G); the GEOFON Network (GE) and the Pacific21 Network (PS). We thank Laura Parisi for initial discussions and also Michael Frietsch and Lewis Schardong for their technical help. EK would like to thank the National Environmental Research Council (NE/L002485/1) for funding this project. AMGF is grateful for support from NERC grants NE/K005669/1 and NE/N011791/1. SJC was supported by the National Research Foundation of Korea (NRF) grant funded by the Korean government (MSIT) (2019R1A2C208506111) and by Basic Science Research Program through the National Research Foundation of Korea (NRF) funded by the Ministry of Education (2019R1A6A1A030-33167). Synthetic seismograms were computed on Archer, the UKs National Supercomputing Service and Shaheen, the supercomuting service of KAUST.

References

Akcelik, V., Bielak, J., Biros, G., Epanomeritakis, I., Ghattas, O., Kim, E. U. I. J., Opez, J. L., Andez, F., Tu, T., and Urbanic, J. (2003). High resolution forward and inverse earthquake modeling on terascale computers. *Proc. ACM/IEEE SC2003 Conference (SC'03)*, Arizona.

Auer, L., Becker, T. W., Boschi, L., and Schmerr, N. (2015). Thermal structure, radial anisotropy, and dynamics of oceanic boundary layers. *Geophysical Research Letters*, 42:9740–9749.

Auer, L., Boschi, L., Becker, T., Nissen-Meyer, T., and Giardini, D. (2014). Savani: A variable resultion whole-mantle model of anisotropic shear velocity variations based on multiple data sets. *Journal of Geophysical Research: Solid Earth*, 119:3006–3034.

Baba, K., Chave, A. D., Evans, R. L., Hirth, G., and Mackie, R. L. (2006). Mantle dynamics beneath the East Pacific Rise at 17S : Insights from the Mantle Electromagnetic and Tomography (MELT) experiment. *Journal of Geophysical Research*, 111:1–18.

Ballmer, M. D., Conrad, C. P., Smith, E. I., and Harmon, N. (2013). Non-hotspot volcano chains produced by migration of shear-driven upwelling toward the East Pacific Rise. *Geology*, 41(4):479–482.

Ballmer, M. D., Ito, G., Hunen, J. V., and Tackley, P. J. (2010). Small-scale sublithospheric convection reconciles geochemistry and geochronology of 'Superplume' volcanism in the western and south Pacific. *Earth and Planetary Science Letters*, 290(1-2):224–232.

Bassin, C., Laske, G., and Masters, G. (2000). The current limits of resolution for surface wave tomography in North America. In *Eos Trans AGU*, volume 81, page F897.

Beghein, C., Xing, Z., and Goes, S. (2019). Thermal nature and resolution of the lithosphere-asthenosphere boundary under the Pacific from surface waves. *Geophysical Journal International*, 216:1441–1465.

Beghein, C., Yuan, K., Schmerr, N., and Xing, Z. (2014). Changes in Seismic Anisotropy Shed Light on the Nature of the Gutenberg Discontinuity. *Science*, 343:1237–1240.

Bozdag, E., Peter, D., Lefebvre, M., Komatitsch, D., Tromp, J., Hill, J., Podhorszki, N., and Pugmire, D. (2016). Global adjoint tomography: first-generation model. *Geophysical Journal International*, 207:1739–1766.

Bozdag, E. and Trampert, J. (2010). Assessment of tomographic mantle models using spectral element seismograms. *Geophysical Journal International*, 180:1187–1199.

Burgos, G., Montagner, J.-P., Beucler, E., Capdeville, Y., Mocquet, A., and Drilleau, M. (2014). Oceanic lithosphere-asthenosphere boundary from surface wave dispersion data. *Journal of Geophysical Research: Solid Earth*, 119:1079–1093.

Capdeville, Y. (2005). An efficient Born normal mode method to compute sensitivity kernels and synthetic seismograms in the Earth. *Geophysical Journal International*, 63:639–646.

Cara, M. and Lévêque, J. J. (1988). Anisotropy of the asthenosphere: The higher mode data of the Pacific revisited. *Geophysical Research Letters*, 15(3):205–208.

Chang, S.-J., Ferreira, A. M. G., Ritsema, J., van Heijst, H. J., and Woodhouse, J. H. (2014). Global radially anisotropic mantle structure from multiple datasets: A review, current challenges, and outlook. *Tectonophysics*, 617:1–19.

Chang, S.-J., Ferreira, A. M. G., Ritsema, J., van Heijst, H. J., and Woodhouse, J. H. (2015). Joint inversion for global isotropic and radially anisotropic mantle structure including crustal thickness perturbations. *Journal of Geophysical Research: Solid Earth*, 120(6):4278–4300.

Chen, M., Niu, F., Liu, Q., Tromp, J., and Zheng, X. (2015). Multiparameter adjoint tomography of the crust and upper mantle beneath East Asia: 1. Model construction and comparisons. *Journal of Geophysical Research*, 120(3):1762–1786.

Chen, M., Tromp, J., Helmberger, D., and Kanamori, H. (2007a). Waveform modeling of the slab beneath Japan. *Journal of Geophysical Research*, 112:1–19.

Chen, P., Jordan, T. H., and Zhao, L. (2007b). Full three-dimensional tomography: a comparison between the scattering-integral and adjoint-wavefield methods. *Geophysical Journal International*, 170:175–181.

Chu, R., Helmberger, D., and Gurnis, M. (2014). Upper mantle surprises derived from the recent Virginia earthquake waveform data. *Earth and Planetary Science Letters*, 402:167–175.

Chu, R., Schmandt, B., and Helmberger, D. V. (2012). Juan de Fuca subduction zone from a mixture of tomography and waveform modeling. *Journal of Geophysical Research*, 117:1–23.

Cochran, J. R. (1986). Variations in subsidence rates along intermediate and fast spreading mid-ocean ridges. *Geophysical Journal of the Royal Astronomical Society*, 87:421–454.

Conder, J. A., Forsyth, D. W., and Parmentier, E. M. (2002). Asthenospheric flow and asymmetry of the East Pacific Rise, MELT area. *Journal of Geophysical Research*, 107(B12):2344.

Dunn, R. A. and Forsyth, D. W. (2003). Imaging the transition between the region of mantle melt generation and the crustal magma chamber beneath the southern East Pacific Rise with short-period Love waves. *Journal of Geophysical Research*, 108:1–20.

Eakin, C. M. and Long, M. D. (2013). Complex anisotropy beneath the Peruvian flat slab from frequency- dependent, multiple-phase shear wave splitting analysis. *Journal of Geophysical Research: Solid Earth*, 118:4794–4813.

Eakin, C. M., Long, M. D., Beck, S. L., Wagner, L. S., Tavera, H., and Condori, C. (2014). Response of the mantle to flat slab evolution: Insights from local S splitting beneath Peru. *Geophysical Research Letters*, 41:3438–3446.

Eakin, C. M., Long, M. D., Wagner, L. S., Beck, S. L., and Tavera, H. (2015). Upper mantle anisotropy beneath Peru from SKS splitting: Constraints on flat slab dynamics and interaction with the Nazca Ridge. *Earth and Planetary Science Letters*, 412:152–162.

Ekström, G. and Dziewoński, A. M. (1998). The unique anisotropy of the Pacific upper mantle. *Nature*, 394(6689):168–172.

Evans, R. L., Tarits, P., Chave, A. D., White, A., Heinson, G., Filloux, J. H., Toh, H., Seama, N., Utada, H., Booker, J. R., and Unsworth, M. J. (1999). Asymmetric electrical structure in the mantle beneath the East Pacific Rise at 17°S. *Science*, 286:752–757.

Faccenda, M., Ferreira, A. M. G., Tisato, N., Lithgow-Bertelloni, C., Stixrude, L., and Pennacchioni, G. (2019). Extrinsic Elastic Anisotropy in a Compositionally Heterogeneous Earth's Mantle. *Journal of Geophysical Research*, 124:1671–1687.

Ferreira, A. M. G., Woodhouse, J. H., Visser, K., and Trampert, J. (2010). On the robustness of global radially anisotropic surface wave tomography. *Journal of Geophysical Research: Solid Earth*, 115:B04313.

Fichtner, A., Kennett, B. L. N., Igel, H., and Bunge, H.-P. (2009). Full seismic waveform tomography for upper-mantle structure in the Australasian region using adjoint methods. *Geophysical Journal International*, 179:1703–1725.

Forsyth, D. W., Webb, S. C., and Dorman, L. M. (1998). Phase velocities of Rayleigh waves in the MELT Experiment on the East Pacific Rise. *Science*, 280:1235–1238.

French, S., Lekić, V., and Romanowicz, B. (2013). Waveform tomography reveals channeled flow at the base of the oceanic asthenosphere. *Science*, 342:227–230.

French, S. W. and Romanowicz, B. A. (2014). Whole-mantle radially anisotropic shear velocity structure from spectral-element waveform tomography. *Geophysical Journal International*, 199:1303–1327.

Gilbert, F. (1971). Excitation of the normal modes of the Earth by earthquake sources. *Geophysical Journal of the Royal Astronomical Society*, 22:223–226.

Grevemeyer, I. (2020). Upper mantle structure beneath the Mid-Atlantic Ridge from regional waveform modeling. *Bulletin of the Seismological Society of America*, 110:18–25.

Gu, Y. J., Lerner-Lam, A. L., Dziewoński, A. M., and Ekström, G. (2005). Deep structure and seismic anisotropy beneath the East Pacific Rise. *Earth and Planetary Science Letters*, 232:259–272.

Gung, Y., Panning, M., and Romanowicz, B. (2003). Global anisotropy and the thickness of continents. *Nature*, 422:707–711.

Harmon, N., Forsyth, D. W., Weeraratne, D. S., Yang, Y., and Webb, S. C. (2011). Mantle heterogeneity and off axis volcanism on young Pacific lithosphere. *Earth and Planetary Science Letters*, 311(3-4):306–315.

Isse, T., Kawakatsu, H., Yoshizawa, K., Takeo, A., Shiobara, H., Sugioka, H., Ito, A., Suetsugu, D., and Reymond, D. (2019). Surface wave tomography for the Pacific Ocean incorporating seafloor seismic observations and plate thermal evolution. *Earth and Planetary Science Letters*, 510:116–130.

Karato, S. (2008). Insights into the nature of plume-asthenosphere interaction from central Pacific geophysical anomalies. *Earth and Planetary Science Letters*, 274(1):234–240.

Kawakatsu, H. (2016). Pacific array of, by and for global deep earth research. *AGU Fall Meeting Abstracts*, DI23C-01.

Kendall, J. M. and Silver, P. G. (1996). Constraints from seismic anisotropy on the nature of the lowermost mantle. *Nature*, 8:409–412.

Komatitsch, D. and Tromp, J. (2002). Spetral-element simulations of global seismic wave propagation, II. Three-dimensional models, oceans, rotation, and self-gravitation. *Geophys. J. Int.*, 150:303–318.

Komatitsch, D. and Vilotte, J.-P. (1998). The spectral element method: An efficient tool to simulate the seismic response of 2D and 3D geological structures. *Bulletin of the Seismological Society of America*, 88(2):368–392.

Kustowski, B., Ekström, G., and Dziewoński, A. M. (2008). Anisotropic shear-wave velocity structure of the Earth's mantle: A global model. *Journal of Geophysical Research: Solid Earth*, 113:B06306.

Lentas, K., Ferreira, A. M. G., and Vallee, M. (2013). Assessment of SCARDEC source parameters of global large ($M_w \geq 7.5$) subduction earthquakes. *Geophysical Journal International*, 195:1989–2004.

Lin, P.-y. P., Gaherty, J. B., Jin, G., Collins, J. A., Lizarralde, D., Evans, R. L., and Hirth, G. (2016). High-resolution seismic constraints on flow dynamics in the oceanic asthenosphere. *Nature*, 535:538–541.

Montagner, J.-P. and Tanimoto, T. (1991). Global upper mantle tomography of seismic velocities and anisotropies. *Journal of Geophysical Research*, 96(B12):20337–20351.

Morgan, J. P. (1987). Melt migration beneath mid-ocean spreading centres. *Geophysical Research Letters*, 14(12):1238–1241.

Morgan, J. P., Morgan, J., Zhang, Y.-S., and Smith, W. H. (1995). Observational hints for a plume-fed, suboceanic asthenosphere and its role in mantle convection. *Journal of Geophysical Research*, 100(B7):12,753–12,767.

Morgan, J. P. and Smith, W. H. (1992). Flattening of the sea-floor depth-age curve as a response to asthenospheric flow. *Nature*, 359:524–527.

Moulik, P. and Ekström, G. (2014). An anisotropic shear velocity model of the Earth's mantle using normal modes, body waves, surface waves and long-period waveforms. *Geo-*

physical Journal International, 199(3):1713–1738.

Nettles, M. and Dziewoński, A. M. (2008). Radially anisotropic shear velocity structure of the upper mantle globally and beneath North America. *Journal of Geophysical Research: Solid Earth*, 113:B02303.

Ni, S., Ding, X., Helmberger, D. V., and Gurnis, M. (1999). Low-velocity structure beneath Africa from forward modeling. *Earth and Planetary Science Letters*, 170:497–507.

Nicolas, A. and Christensen, N. (1987). *Formation of anisotropy in upper mantle peridotites: a review.* AGU, Washington, D.C.

Nishimura, C. E. and Forsyth, D. W. (1989). The anisotropic structure of the upper mantle in the Pacific Ocean. *Geophysical Journal*, 96:203–229.

Olsen, K. B., Day, S. M., and Bradley, C. R. (2003). Estimation of Q for long-leriod (>2 sec) waves in the Los Angeles Basin. *Bulletin of the Seismological Society of America*, 93(2):627–638.

Olsen, K. B., Pechmann, J. C., and Schuster, G. T. (1995). Simulation of 3D elastic wave propagation in the Salt Lake Basin. *Bulletin of the Seismological Society of America*, 85(6):1688–1710.

Parisi, L. and Ferreira, A. M. G. (2016). Empirical assessment of the validity limits of the surface wave full ray theory using realistic 3-D Earth models. *Geophys. J. Int.*, 205:146–159.

Parisi, L., Ferreira, A. M. G., and Ritsema, J. (2018). Apparent splitting of S waves propagating through an isotropic lowermost mantle. *Journal of Geophysical Research*, 123:3909–3922.

Qin, Y., Capdeville, Y., Maupin, V., Montagner, J.-p., Lebedev, S., and Beucler, E. (2008). SPICE benchmark for global tomographic methods. *Geophys. J. Int.*, 175:598–616.

Qin, Y., Capdeville, Y., Montagner, J.-P., Boschi, L., and Becker, T. W. (2009). Reliability of mantle tomography models assessed by spectral element simulation. *Geophys. J. Int.*, 177:125–144.

Ritsema, J., Deuss, A., van Heijst, H. J., and Woodhouse, J. H. (2011). S40RTS: a degree-40 shear-velocity model for the mantle from new Rayleigh wave dispersion, teleseismic traveltime and normal-mode splitting function measurements. *Geophysical Journal International*, 184(3):1223–1236.

Ritzwoller, M. H. and Levshin, A. L. (1998). Eurasian surface wave tomography: Group velocities. *Journal of Geophysical Research*, 103(B3):4839–4878.

Rychert, C. A., Laske, G., Harmon, N., and Shearer, P. M. (2013). Seismic imaging of melt in a displaced Hawaiian plume. *Nature Geoscience*, 6(8):657–660.

Schmerr, N. (2012). The Gutenberg discontinuity: Melt at the lithosphere-asthenosphere boundary. *Science*, 335:1480–1483.

Tan, Y. and Helmberger, D. V. (2007). Trans-Pacific upper mantle shear velocity structure. *Journal of Geophysical Research*, 112:B08301.

Tape, C., Liu, Q., Maggi, A., and Tromp, J. (2009). Adjoint tomography of the southern California crust. *Science*, 325:988–993.

Thorne, M. S., Zhang, Y., and Ritsema, J. (2013). Evaluation of 1-D and 3-D seismic models of the Pacific lower mantle with S, SKS, and SKKS traveltimes and amplitudes. *Journal of Geophysical Research*, 118:1–11.

Toomey, D. R., Wilcock, W. S. D., Conder, J. A., Forsyth, D. W., Blundy, J. D., Parmentier, E. M., and Hammond, W. C. (2002). Asymmetric mantle dynamics in the MELT region of the East Pacific Rise. *Earth and Planetary Science Letters*, 200:287–295.

Toomey, D. R., Wilcock, W. S. D., Solomon, S. C., Hammond, W. C., and Orcutt, J. A. (1998). Mantle seismic structure beneath the MELT region of the East Pacific Rise from P and S wave tomography. *Science*, 280:1224–1227.

Visser, K., Trampert, J., Lebedev, S., and Kennett, B. L. N. (2008). Probability of radial anisotropy in the deep mantle. *Earth and Planetary Science Letters*, 270(34):241–250.

Wang, N., Montagner, J.-p., Fichtner, A., and Capdeville, Y. (2013). Intrinsic versus extrinsic seismic anisotropy: The radial anisotropy in reference Earth models. *Geophysical Research Letters*, 40:4284–4288.

Weeraratne, D. S., Forsyth, D. W., Yang, Y., and Webb, S. C. (2007). Rayleigh wave tomography beneath intraplate volcanic ridges in the South Pacific. *Journal of Geophysical Research*, 112:1–18.

Wolfe, C. J. and Solomon, S. C. (1998). Shear-wave splitting and implications for mantle flow beneath the MELT region of the East Pacific Rise. *Science*, 280:1230–1233.

Woodhouse, J. H. and Dziewonski, A. M. (1984). Mapping the upper mantle: Three-dimensional modeling of earth structure by inversion of seismic waveforms. *Journal of Geophysical Research: Solid Earth*, 89:5953–5986.

Zhang, S. and Karato, S. (1995). Lattice preferred orientation of olivine aggregates deformed in simple shear. *Nature*, 375:774–777.

Event Code	Region	Date	Mw	Depth (km)	Latitude (°)	Longitude (°)
200507100446A	West Chile Rise	10/07/2005	6.0	12	-36.35	-97.25
200512221220A	Pacific-Antarctic Ridge	22/12/2005	6.4	15	-54.61	-135.95
200610151707A	Hawaii	15/10/2006	6.7	48	19.88	-156.12
200708140538A	Hawaii	14/08/2007	5.4	12	19.30	155.18
071104C	South Pacific Ocean	11/07/2004	6.1	14	-20.17	-126.91
201001171200A	Drake Passage	17/01/2010	6.2	19	-57.69	-66.04
201002050659A	Southeast Indian Ridge	05/02/2010	6.2	12	-47.93	99.51
201007042155A	Near East Coast Of Honshu, Japan	04/07/2010	6.3	35	39.66	142.80
201008132119A	South Of Mariana Islands	13/08/2010	6.9	12	12.47	141.56
201012020312A	New Britain Region, P.N.G.	02/12/2010	6.6	49	-6.10	149.92
201105130336A	Pacific-Antarctic Ridge	13/05/2011	5.7	15	-59.48	-151.17
201109231902A	Central East Pacific Rise	23/09/2011	5.9	16	-9.16	-109.55
201110070858A	South Of Kermadec Islands	07/10/2011	6.1	49	-32.42	-178.80
201111021459A	Pacific-Antarctic Ridge	02/11/2011	6.2	15	-55.11	-128.92
201210091232A	West Of Macquarie Island	09/10/2012	6.5	21	-60.64	153.93
201301302015A	Central Chile	30/01/2013	6.8	46	-28.11	-70.89
201306050012A	Hawaii	05/06/2013	5.2	45	18.90	-155.13
201309111244A	Central East Pacific Rise	11/09/2013	6.0	16	-4.96	-104.81
201310191754A	Gulf Of California	19/10/2013	6.6	16	25.96	-110.36
201404240310A	Vancouver Island	24/04/2014	6.6	17	49.65	-127.65
201405142056A	E. Caroline Islands, Micronesia	14/05/2014	6.2	27	6.37	144.94
201410090214A	Southern East Pacific Rise	09/10/2014	7.0	12	-32.11	-110.81
201504130353A	North Pacific Ocean	13/04/2015	5.0	20	17.24	-121.89
201505191525A	Pacific-Antarctic Ridge	19/05/2015	6.6	15	-54.33	-132.16
201507180227A	Santa Cruz Islands	18/07/2015	6.9	12	-10.46	165.10
201511132051B	Northwest of Ryukyu Islands	13/11/2015	6.7	12	31.00	28.87
201601311739A	Balleny Islands Region	31/01/2016	6.0	12	-63.29	169.15
201602162348A	Southern East Pacific Rise	16/02/2016	6.1	20	-55.78	-125.17
201604020550A	Alaska Peninsula	02/04/2016	6.2	12	57.00	-157.93
201604281933A	Vanuatu Islands	28/04/2016	7.0	34	-16.04	167.38
201604290133A	Northern East Pacific Rise	29/04/2016	6.6	15	10.28	-103.74
201606080831A	Central East Pacific Rise	08/06/2016	5.9	15	-4.06	-104.55
201611241843A	Off Coast Of Central America	24/11/2016	7.0	12	11.96	-88.84
201706022224A	Near Islands, Aleutian Islands	02/06/2017	6.8	13	54.03	170.91
201710181200A	Tonga Islands	18/10/2017	6.1	17	-20.59	-173.80
201802021137A	Pacific-Antartic Ridge	02/02/2018	6.0	12	-65.81	-175.64
201805180145A	South Of Kermadec Islands	18/05/2018	6.1	14	-34.59	-178.41

Table 1. Event information (event code, region, date, magnitude, depth, latitude and longitude) of the seismic events from the global CMT catalogue (www.globalcmt.org) used in the this study.

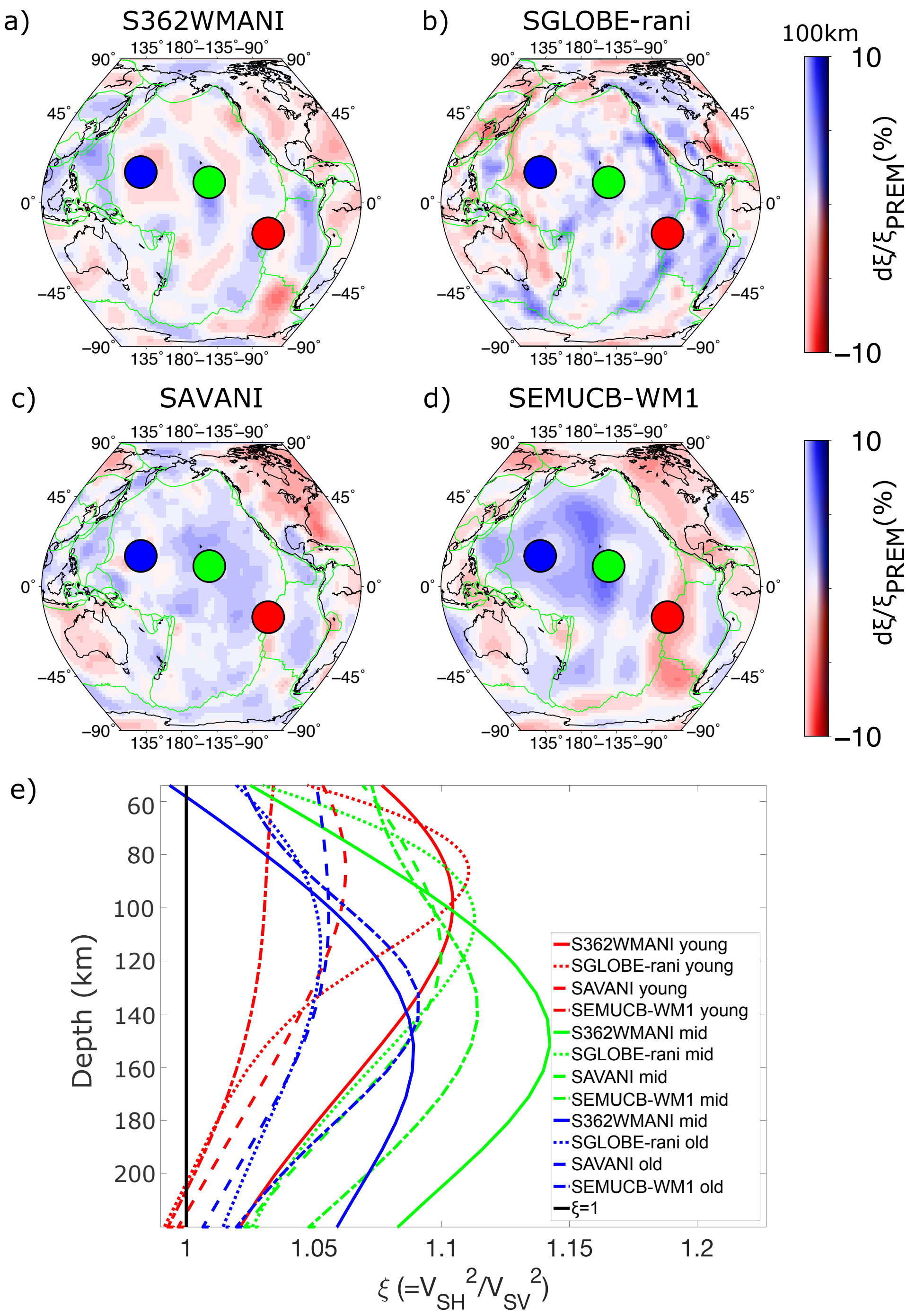

Figure 1. Perturbations with respect to PREM in the radially anisotropic ξ structure of a) S362WMANI (Kustowski et al., 2008), b) SGLOBE-rani (Chang et al., 2015), c) SAVANI (Auer et al., 2014) and d) SEMUCB-WM1 (French and Romanowicz, 2014) at 100 km depth. e) 1-D depth profiles of ξ for S362WMANI [solid lines], SGLOBE-rani [dotted lines], SAVANI [dashed lines] and SEMUCB-WM1 [dashed-dotted lines] beneath young ocean (5 Ma; red dot in a)-d) and curves), mid-age ocean (90 Ma; green dot in a)-d) and curves) and old ocean (170 Ma; blue dot in a)-d) and curves). $\xi = 1$ is indicated by a vertical black line for reference.

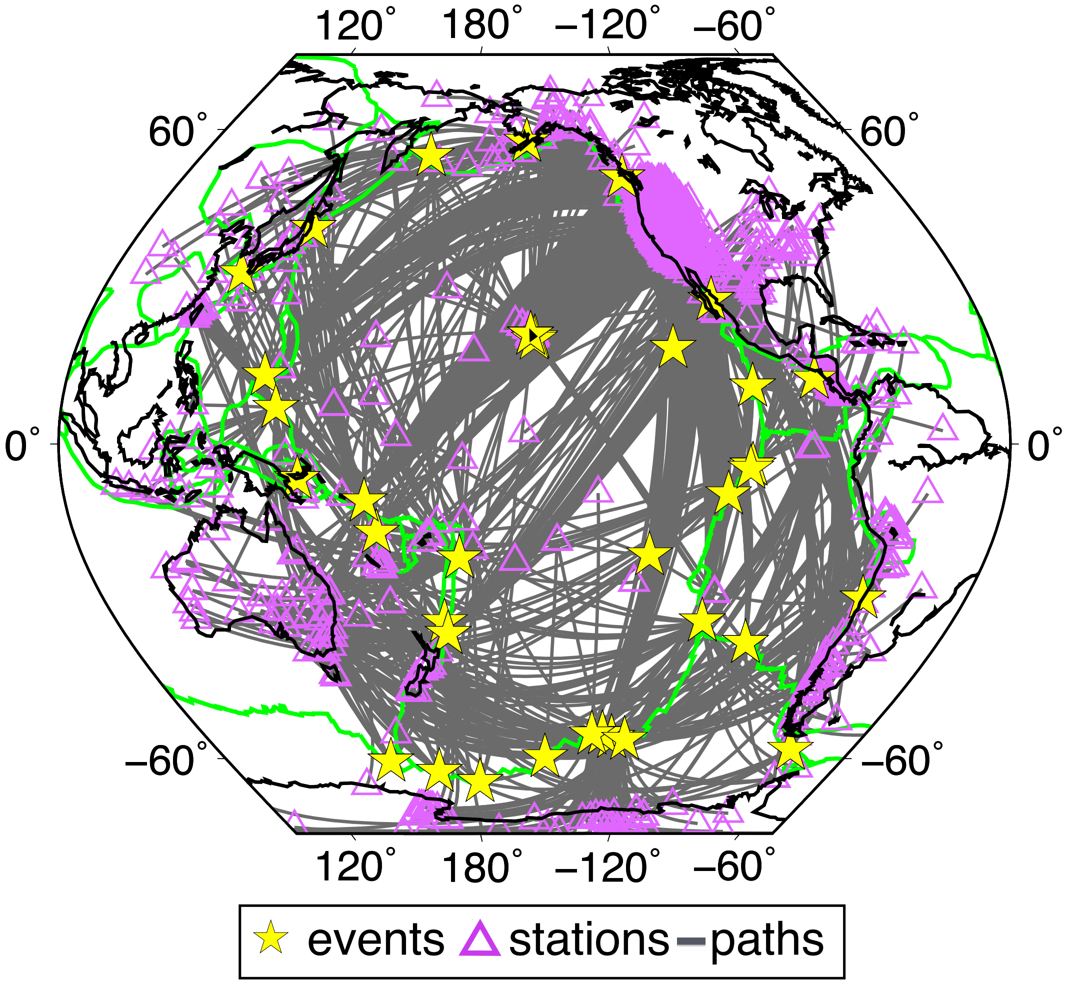

Figure 2. Pacific dataset comprising 2,307 great-circle paths (grey) from 36 events (yellow stars) in 2005-2017 with Mw 5.0-7.0 and depth 0-50 km recorded at 1,125 different stations (purple triangles) used for phase and amplitude misfit analysis to test various 3-D Earth models in the Pacific.

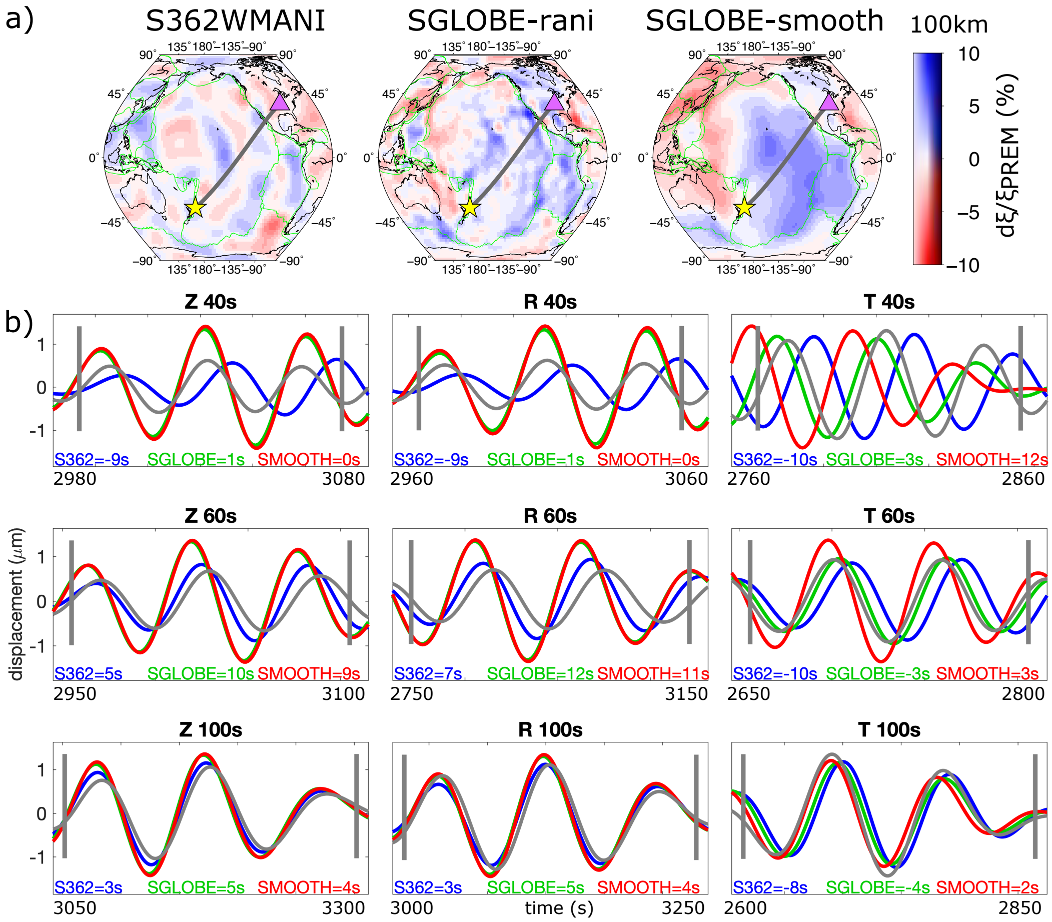

Figure 3. a) Great-circle path from an event in south of the Kermadec islands (event GCMT code: 201805180145A) crossing the Pacific to station T42B in the US for which waveform comparisons are made. Background colors represent perturbations with respect to PREM in the radially anisotropic ξ structure of S362WMANI (Kustowski et al., 2008), SGLOBE-rani (Chang et al., 2015) and SGLOBE-smooth (left to right, respectively) at 100 km depth. b) Waveform comparisons between the data (grey) and synthetics computed for the 3-D mantle models S362WMANI (blue), SGLOBE-rani (green) and SGLOBE-smooth (red). Waveform comparisons are shown for the vertical (Z), radial (R) and transverse (T) components, respectively, at wave periods T$\sim$40 s, 60 s and 100 s (top to bottom). The grey vertical lines show the surface wave windows considered and the phase misfits are shown in the bottom of each subplot for each model considered.

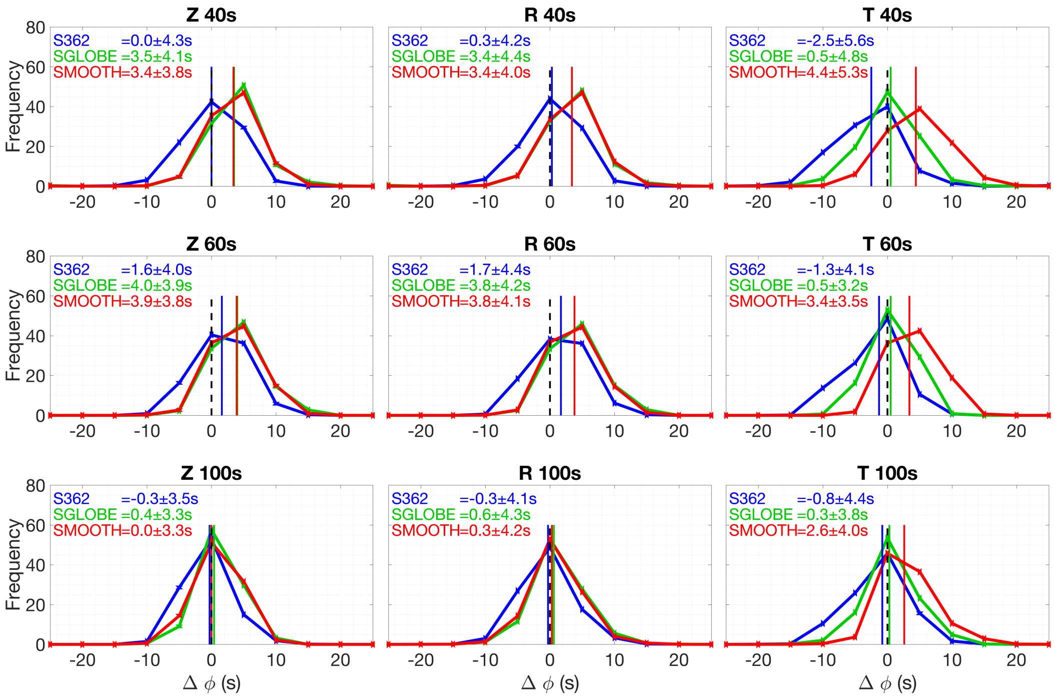

Figure 4. Distributions of phase misfits for the Pacific paths in Fig. 2 for waveforms computed using the Earth models S362WMANI (blue), SGLOBE-rani (green) and SGLOBE-smooth (red) filtered with a dominant wave period of T∼40 s, 60 s and 100 s (top to bottom) for each component (vertical, Z; radial, R; and transverse, T; left to right). A phase misfit of 0 is indicated by a vertical black dashed line for reference. The median and standard deviation can be seen at the top left of each subplot, with the medians also being plotted as vertical colored bars. Positive/negative phase shifts $\Delta\phi$ mean that the synthetic waveforms are faster/slower than the observations.

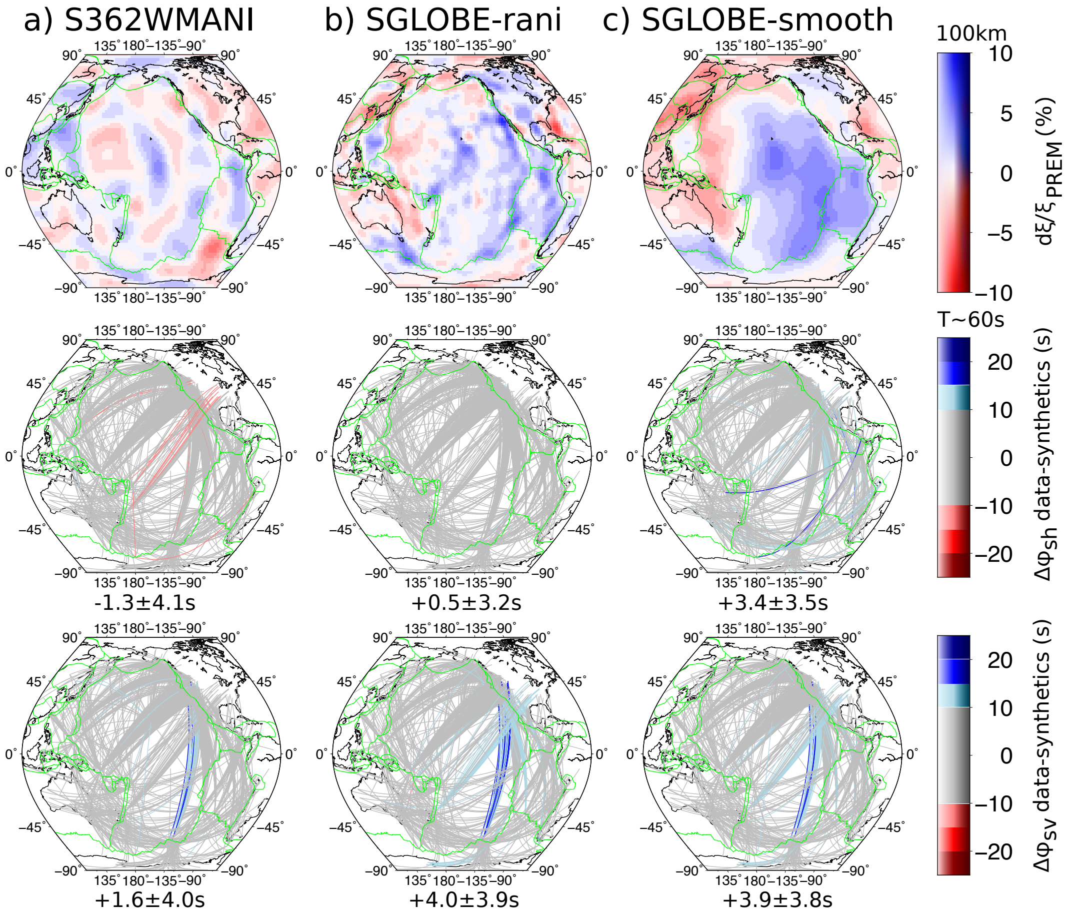

Figure 5. Top row: depth slices of perturbations in radially anisotropic anomalies with respect to PREM at 100 km in the Pacific for a) S362WMANI, b) SGLOBE-rani and c) SGLOBE-smooth. Fundamental mode Love (middle row) and Rayleigh (bottom row) wave phase misfits for waveforms filtered with a dominant wave period of T∼60 s, color-coded for synthetics fitting the data within 10 s (grey), more than 10 s slower than the data (pink-brown), more than 10 s faster than the data (blue). The median and standard deviation for each model are shown at the bottom of each subplot.

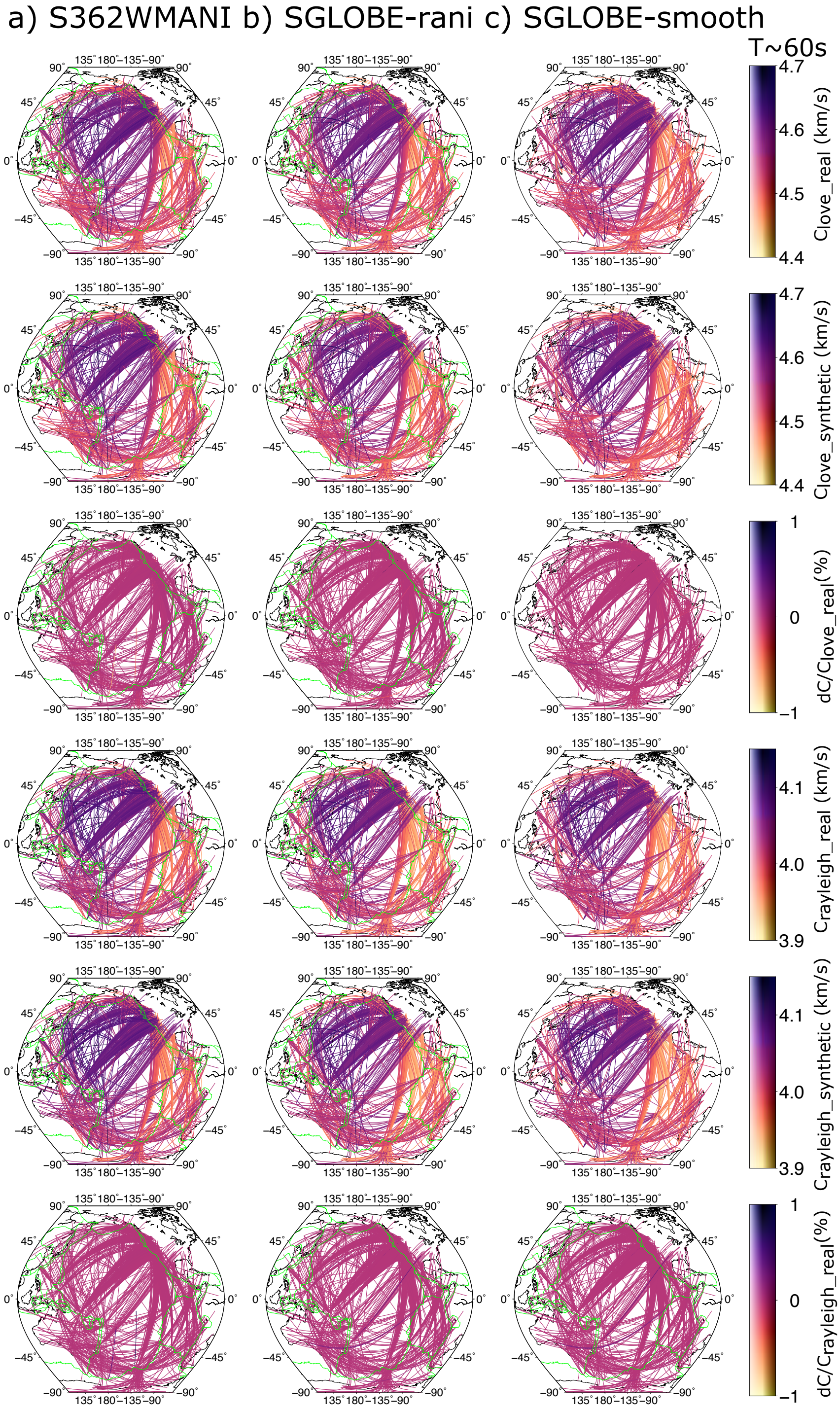

Figure 6. Geographical distribution of real (first row), modified synthetic (second row) Love wave phase velocities and the percentual difference between them (third row) at T∼60 s for a) S362WMANI, b) SGLOBE-rani and c) SGLOBE-smooth. The same format is shown for Rayleigh wave phase velocities (fourth to sixth rows). The percentual differences shown in the third and sixth rows are mostly lower than 0.1%, which shows that our associated estimates of Earth structure lead to a good fit to the data.

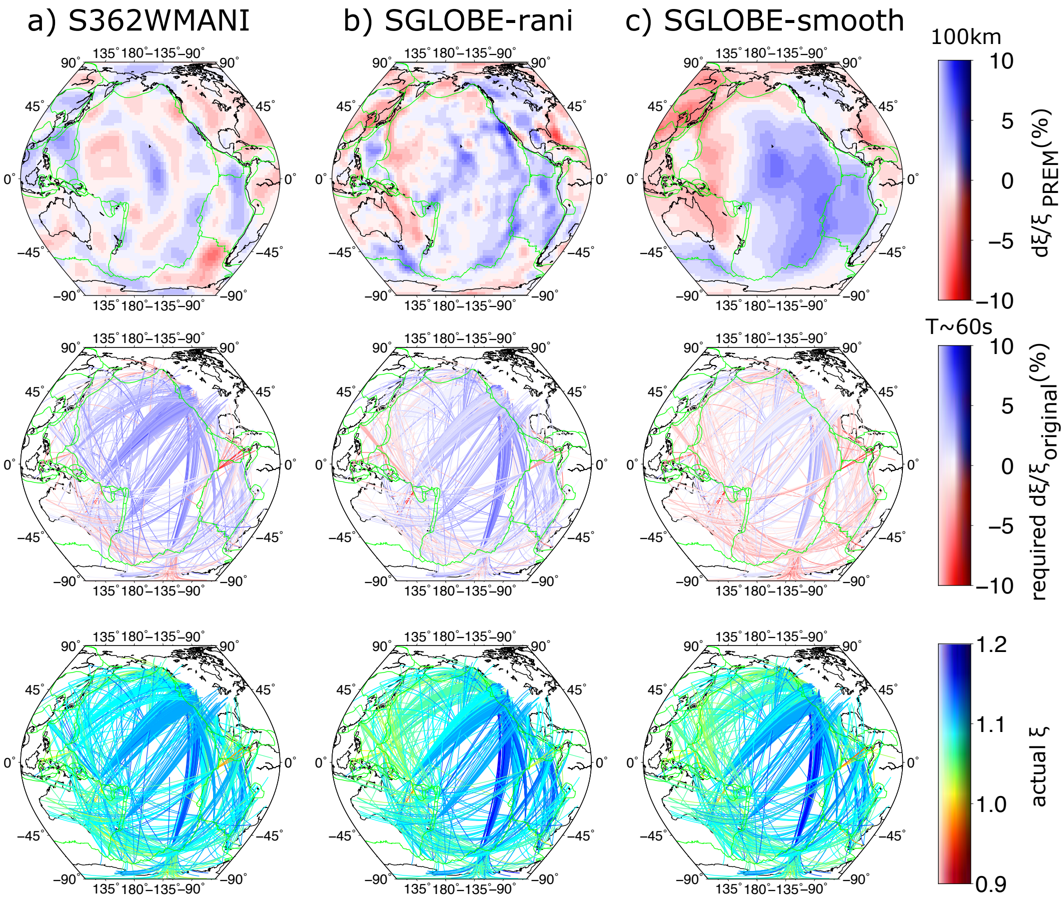

Figure 7. Depth slices of perturbations in radially anisotropic anomalies with respect to PREM at 100 km in the Pacific for a) S362WMANI, b) SGLOBE-rani and c) SGLOBE-smooth can be seen at the top. The adjustments in radial anisotropy required with respect to the original anisotropy are shown in the middle. Blue colors indicate that positive anisotropic anomalies with respect to the original anisotropy are required to fit the data. The required adjustments in radial anisotropy for each model are made and the resulting, adjusted absolute radial anisotropy is shown in the bottom row.

Supplementary information for: Constraints on the upper mantle structure beneath the Pacific from 3-D anisotropic waveform modelling

E. Kendall [1], A.M.G. Ferreira [1,2], S.-J. Chang [3], D. Peter [4]

[1] Department of Earth Sciences, University College London, London, UK 2 CERIS, Instituto Superior Técnico, Universidade de Lisboa, Lisbon, Portugal 3 Division of Geology and Geophysics, Kangwon National University, Chuncheon, South Korea 4 Extreme Computing Research Center, King Abdullah University of Science and Technology (KAUST), Thuwal, Saudi Arabia

Contents of this file

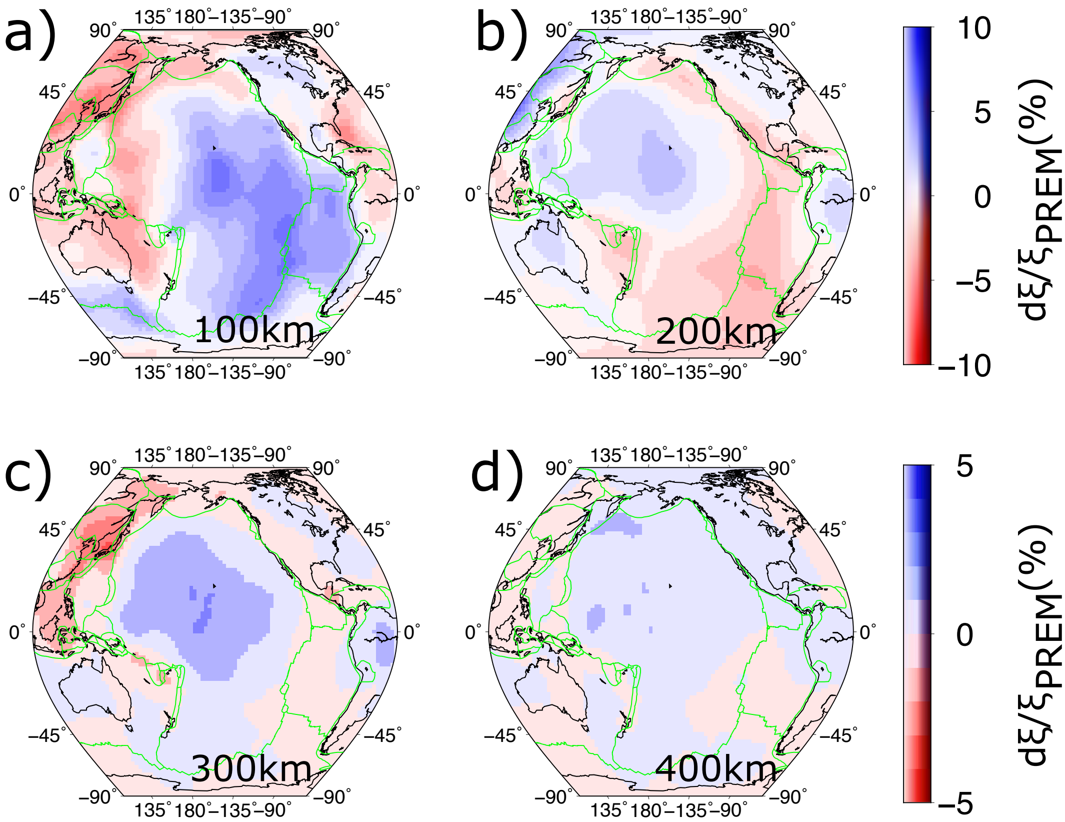

Figure S1. Perturbations with respect to PREM in the radially anisotropic ξ structure of SGLOBE-smooth at a) 100 km, b) 200 km, c) 300 km and d) 400 km depth.

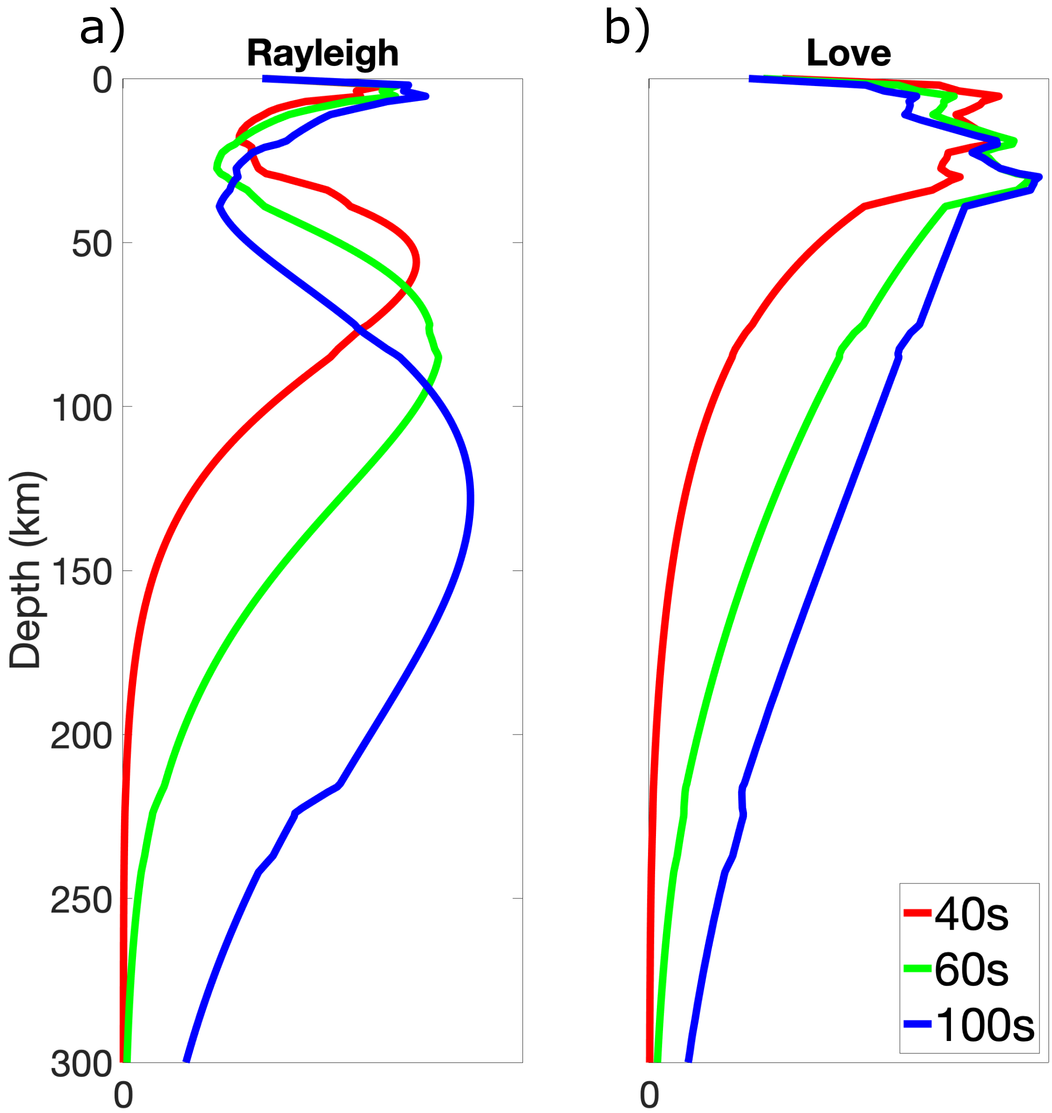

Figure S2. Normalized a) Rayleigh and b) Love wave fundamental mode phase-velocity kernels with respect to the vertically polarized ($\frac{dC}{dV_{SV}}$) and horizontally polarized shear wave ($\frac{dC}{dV_{SH}}$), respectively at wave periods of T$\sim$40 s (red), 60 s (green) and 100 s (blue). The 1D reference model PREM is used to compute the kernels.

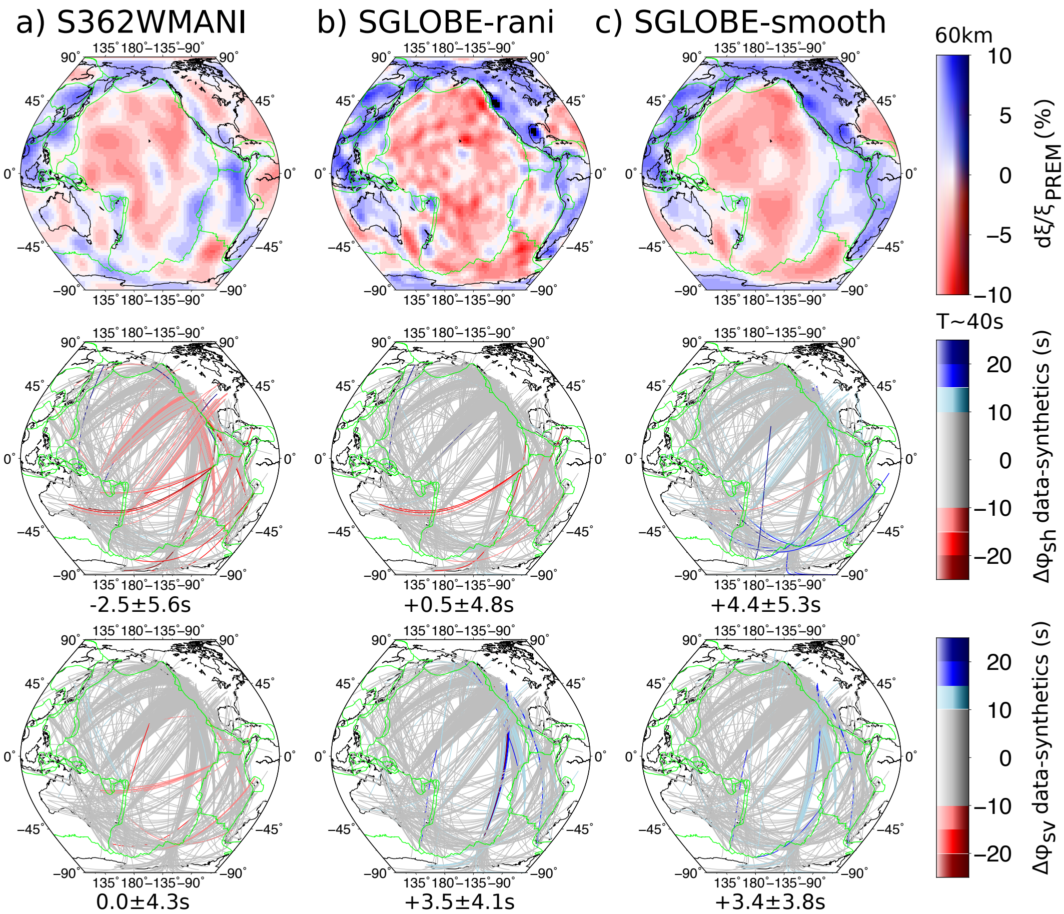

Figure S3. Top row: depth slices of perturbations in radially anisotropic anomalies with respect to PREM at 60 km depth in the Pacific for a) S362WMANI, b) SGLOBE-rani and c) SGLOBE-smooth. Fundamental mode Love (middle row) and Rayleigh (bottom row) wave phase misfits for waveforms filtered with a dominant wave period of T∼40 s, color-coded for synthetics fitting the data within 10 s (grey), more than 10 s slower than the data (pink-brown), more than 10 s faster than the data (blue). The median and standard deviation for each model are shown at the bottom of each subplot.

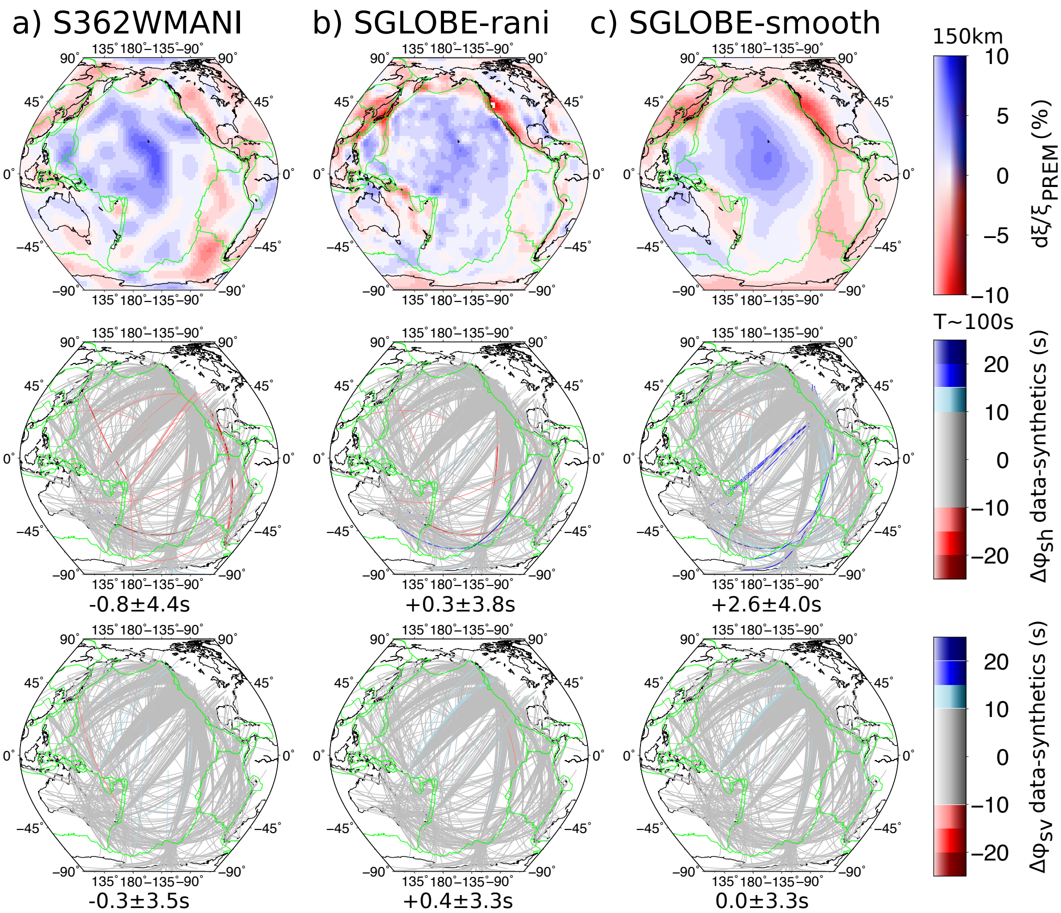

Figure S4. Top row: depth slices of perturbations in radially anisotropic anomalies with respect to PREM at 150 km depth in the Pacific for a) S362WMANI, b) SGLOBE-rani and c) SGLOBE-smooth. Fundamental mode Love (middle row) and Rayleigh (bottom row) wave phase misfits for waveforms filtered with a dominant wave period of T∼100 s, color-coded for synthetics fitting the data within 10 s (grey), more than 10 s slower than the data (pink-brown), more than 10 s faster than the data (blue). The median and standard deviation for each model are shown at the bottom of each subplot.

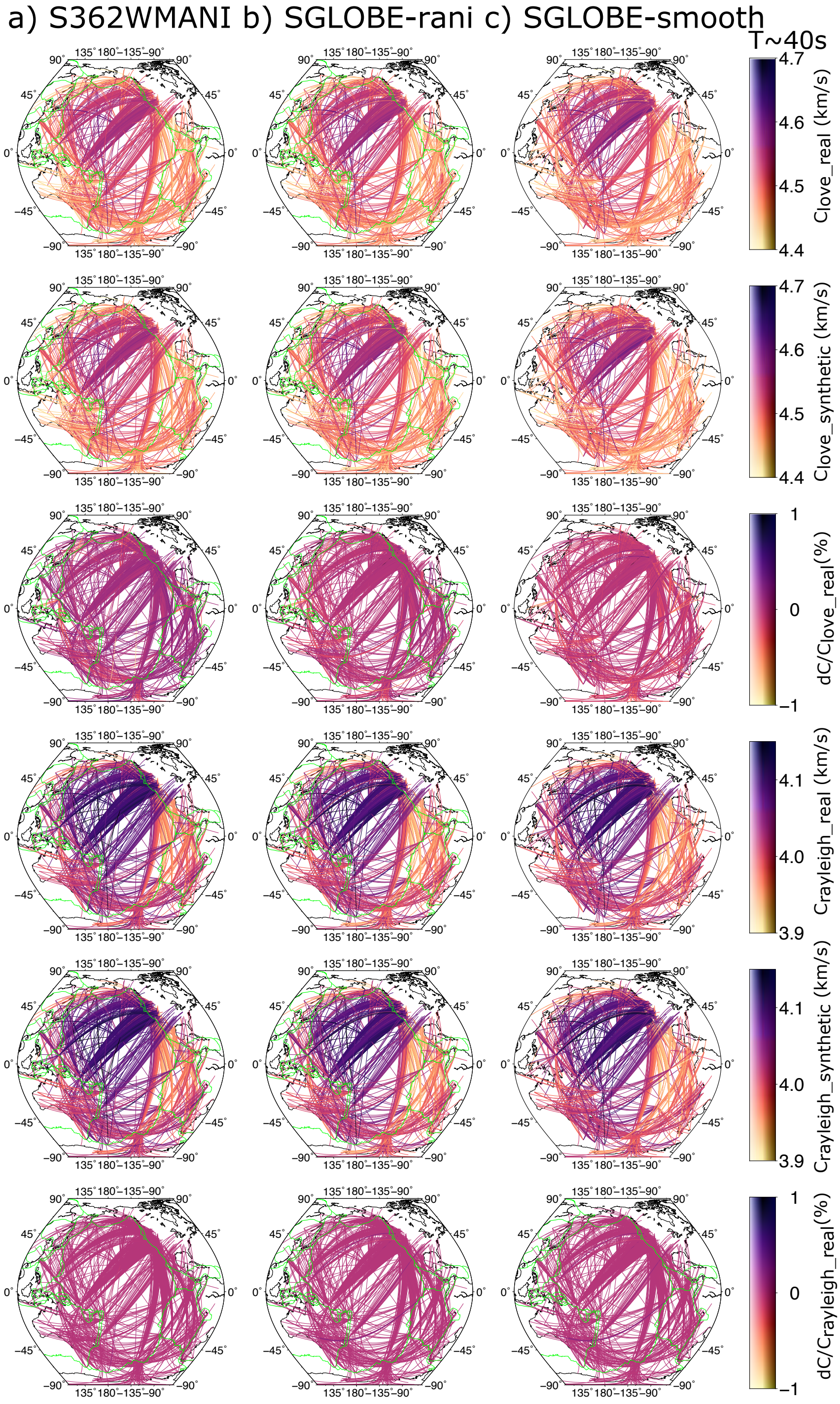

Figure S5. Geographical distribution of real (first row), modified synthetic (second row) Love wave phase velocities and the percentual difference between them (third row) at T∼40 s for a) S362WMANI, b) SGLOBE-rani and c) SGLOBE-smooth. The same format is shown for Rayleigh wave phase velocities (fourth to sixth rows). The percentual differences shown in the third and sixth rows are mostly lower than 0.1%, which shows that our associated estimates of Earth structure lead to a good fit to the data.

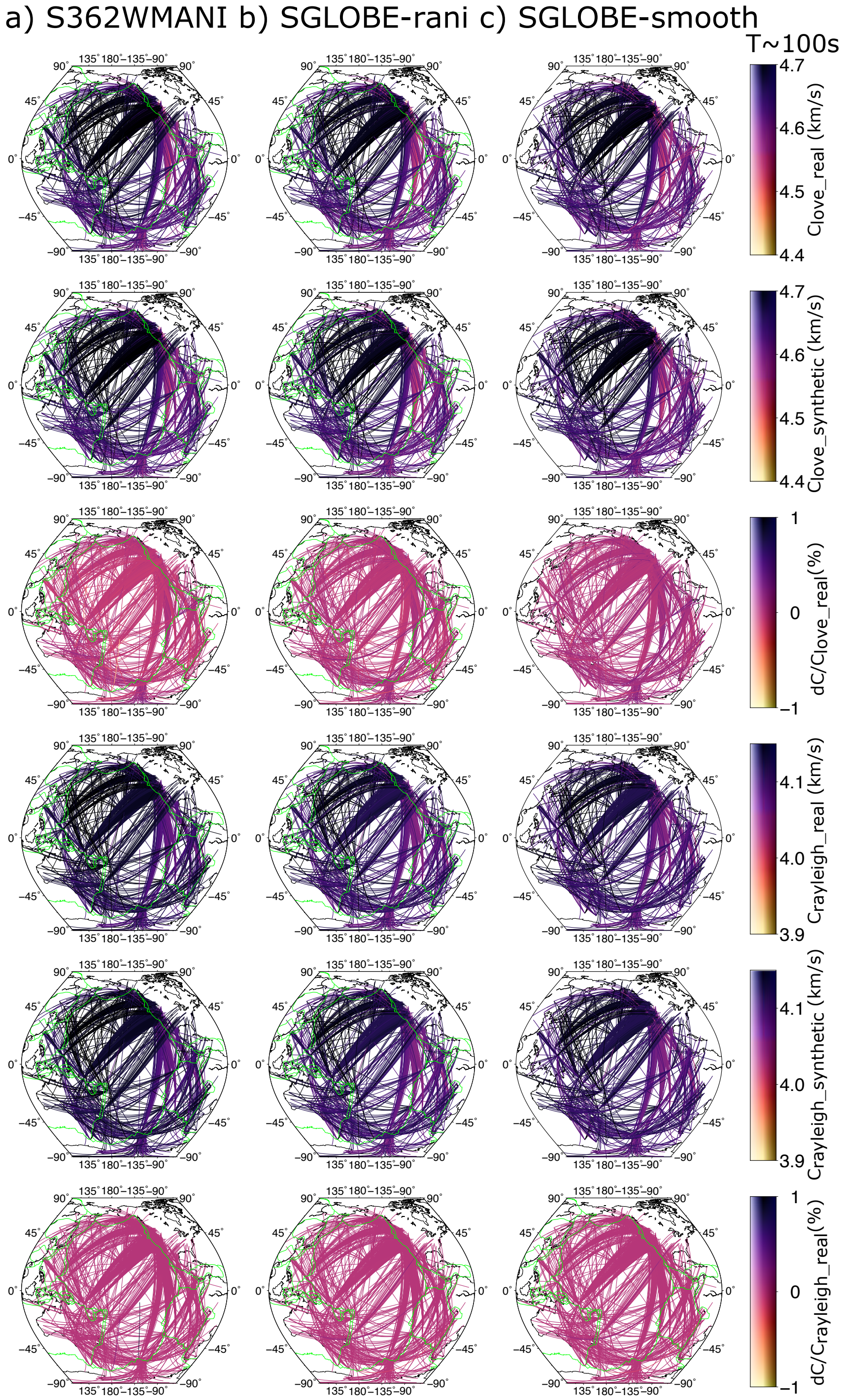

Figure S6. Geographical distribution of real (first row), modified synthetic (second row) Love wave phase velocities and the percentual difference between them (third row) at T$\sim$100 s for a) S362WMANI, b) SGLOBE-rani and c) SGLOBE-smooth. The same format is shown for Rayleigh wave phase velocities (fourth to sixth rows). The percentual differences shown in the third and sixth rows are mostly lower than 0.1%, which shows that our associated estimates of Earth structure lead to a good fit to the data.

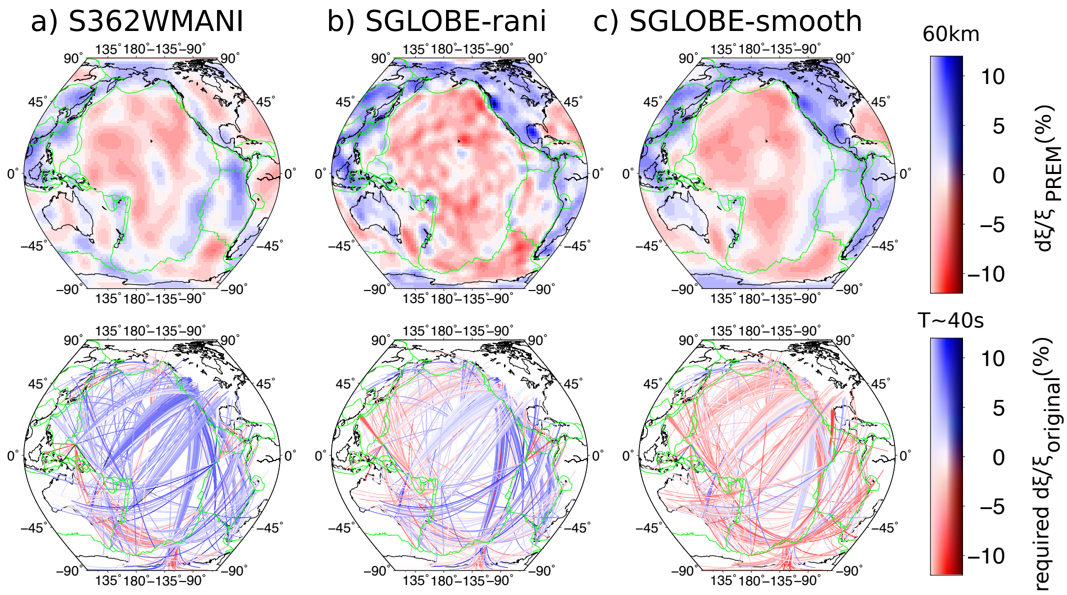

Figure S7. Depth slices of perturbations in radially anisotropic anomalies with respect to PREM at 60 km depth (top) in the Pacific for a) S362WMANI, b) SGLOBE-rani and c) SGLOBE-smooth. The geographical distribution of the required adjustments in radial anisotropy with respect to the original anisotropy are shown in the middle (bottom). Blue (red) colors indicate that positive (negative) anisotropic anomalies with respect to the original anisotropy are required to fit the data.

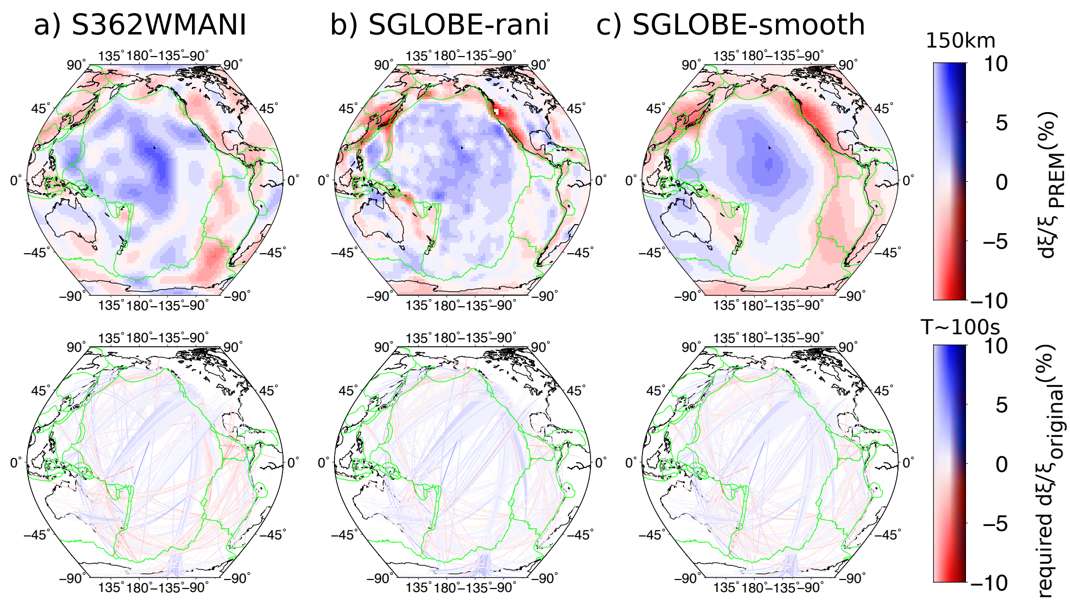

Figure S8. Depth slices of perturbations in radially anisotropic anomalies with respect to PREM at 150 km depth (top) in the Pacific for a) S362WMANI, b) SGLOBE-rani and c) SGLOBE-smooth. The geographical distribution of the required adjustments in radial anisotropy with respect to the original anisotropy are shown in the middle (bottom). Blue (red) colors indicate that positive (negative) anisotropic anomalies with respect to the original anisotropy are required to fit the data.

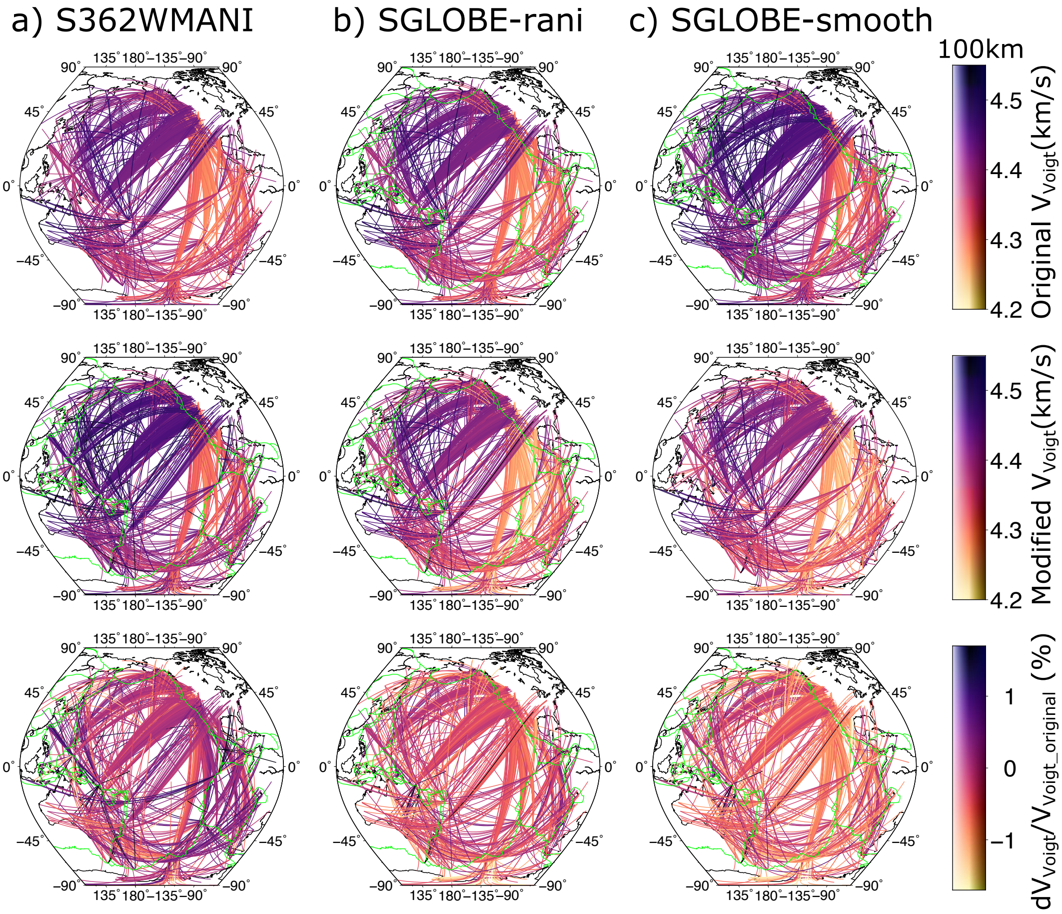

Figure S9. Original (top), modified (middle) and percentage difference between original and modified isotropic V_S structure (Voigt average, V_{Voigt}) (bottom) along path in a) S362WMANI, b) SGLOBE-rani and c) SGLOBE-smooth at ∼100 km depth.

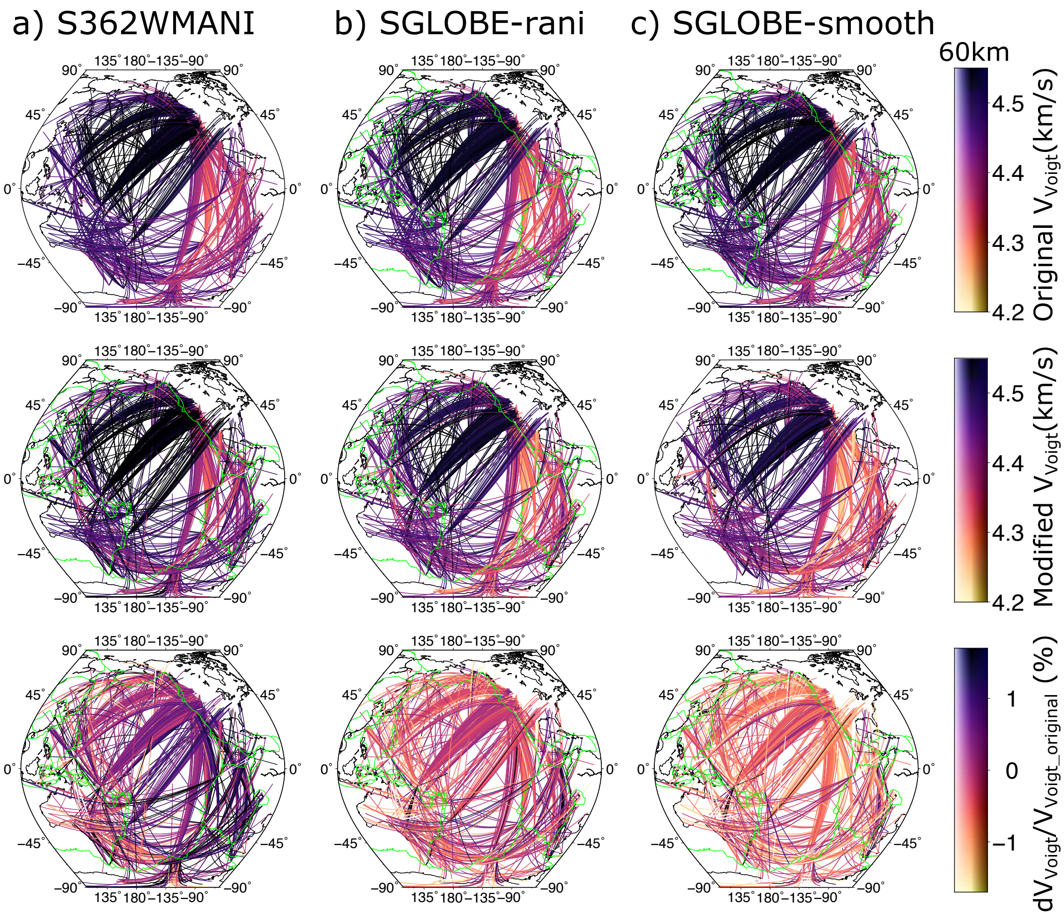

Figure S10. Original (top), modified (middle) and percentage difference between original and modified isotropic V_S structure (Voigt average, V_{Voigt}) (bottom) along path in a) S362WMANI, b) SGLOBE-rani and c) SGLOBE-smooth at ∼60 km depth.

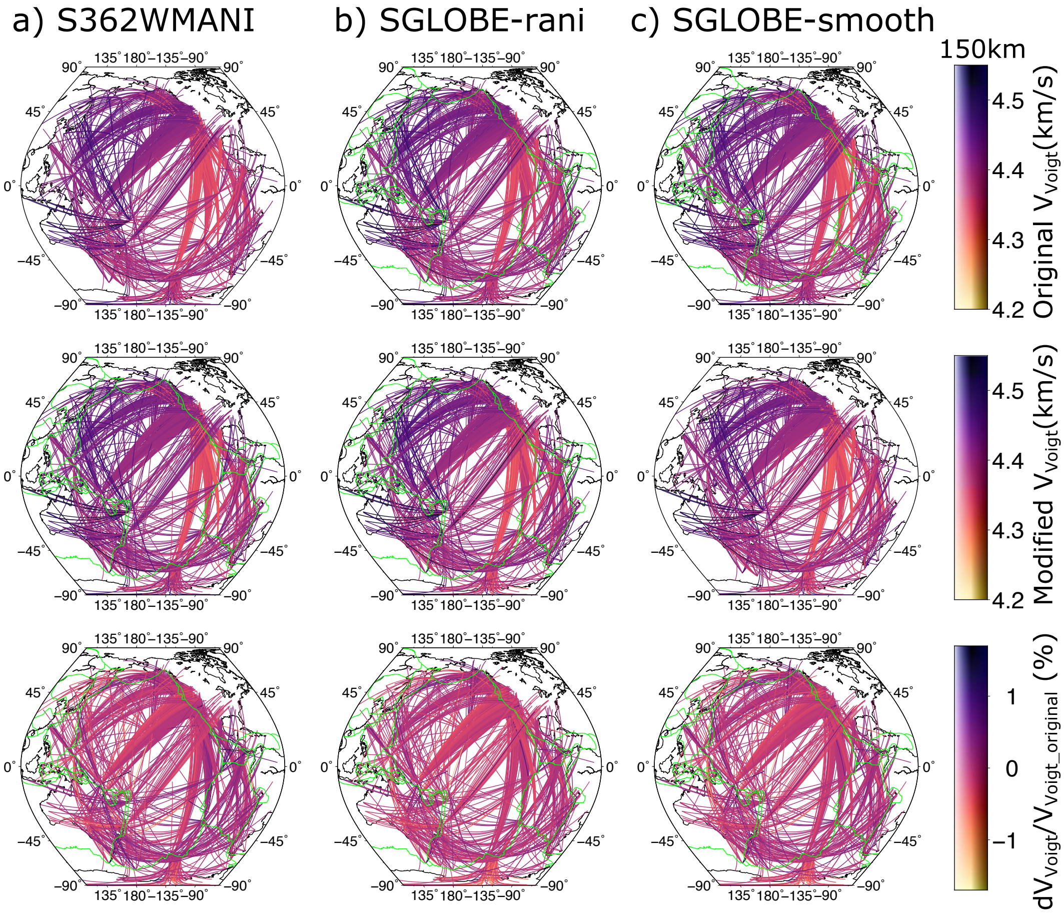

Figure S11. Original (top), modified (middle) and percentage difference between original and modified isotropic V_S structure (Voigt average, V_{Voigt}) (bottom) along path in a) S362WMANI, b) SGLOBE-rani and c) SGLOBE-smooth at ∼150 km depth.